Effect of Domain Topology on the Competing Orders in Strongly Correlated Systems

CHUNRUO DUAN

B.Sc., Peking University, Physics Department, China, 2013

A Dissertation Presented to the Graduate Faculty of the University of Virginia in Candidacy for the Degree of Doctor of Philosophy

DEPARTMENT OF PHYSICS

UNIVERSITY OF VIRGINIA

04/2019

Contents

List of Figures **5**

List of Tables **6**

Acknowledgements **7**

1 Introduction **10**

1.1 Superconductivity 14

1.2 Multiferroics 19

2 Methods **23**

2.1 X-ray/Neutron Scattering 24

2.2 Monte Carlo Simulation 29

3 Neutron Scattering Study on the Coupling of Magnetism and Ferroelectricity in the Hexagonal Multiferroic $RMnO_3$ **32**

3.1 Introduction 33

3.2 Neutron Scattering Results 36

3.3 Summary 39

4 Monte Carlo Simulation on the Coupling of Magnetism and Ferroelectricity in the Hexagonal Multiferroic $RMnO_3$ **40**

4.1 Introduction 41

4.2 Monte Carlo Simulation 43

4.3 Summary 49

5 Neutron and X-ray study on the Fe Vacancy Ordering in Fe-based Superconductor $K_xFe_{2-y}Se_2$ 50

5.1 Introduction 51

5.2 Experimental results 54

5.3 Summary 59

6 Monte Carlo Simulation on the Fe Vacancy Ordering in Fe-based Superconductor $K_xFe_{2-y}Se_2$ 60

6.1 Introduction 61

6.2 Monte Carlo Simulation 62

6.3 Summary 67

7 Discussion 68

7.1 Discussion on the multiferroic $RMnO_3$ 69

7.2 Discussion on the Fe-based Superconductor $K_xFe_{2-y}Se_2$ 71

8 Conclusion 73

Appendix 75

References 77

List of Figures

1.1 Schematic plots illustrating the Hubbard model and the band structure of a Mott insulator. 11

1.2 Schematic plot for the J_1 J_2 Heisenberg model. 11

1.3 Domain topology with competing orders in cuprate superconductors and multiferroic materials. 12

1.4 Schematic phase diagram of type-I and type-II superconductors. 14

1.5 Schematic plots illustrating the electron-phonon coupling described in the BCS theory. 15

1.6 A timeline of the discoveries of superconductors. 16

1.7 Phase diagrams of cuprate and Fe-based superconductors 17

1.8 Schematic plot illustrating the ferroic orders in multiferroic materials. . . 19

1.9 Schematic plot illustrating geometrical frustration. 21

2.1 Schematic plot explaining Bragg's law. 24

2.2 Schematic plot of powder diffraction and a typical powder diffraction pattern of NaCl. 26

2.3 Schematic plot of Laue diffractometer and triple axis spectrometer. . . . 27

2.4 Schematic plot showing 2D Ising model and the simulated magnetic phase transition. 29

2.5 Finite size scaling on the Monte Carlo results of a 2D Ising model. 31

3.1 Crystal structures for high and low temperature $RMnO_3$. 33

3.2 Magnetic structures of hexagonal $RMnO_3$. 34

3.3 Schematic plot showing the experimental setup. 36
3.4 Magnetic order parameter of $LuMnO_3$ extracted from the intensity of (101) and (100) peaks. 36
3.5 Elastic neutron diffraction data on $LuMnO_3$. 37
3.6 Inelastic neutron diffraction data on $LuMnO_3$. 38

4.1 Crystal structures for high and low temperature $RMnO_3$ and the simulated structural domain. 41
4.2 Simulation results on the ferroelectric order parameter of $RMnO_3$. Two transitions were observed. 45
4.3 Simulation results on the magnetic order parameter of $RMnO_3$ under different structural domain distributions. 47

5.1 Crystal structures of $K_xFe_{2-y}Se_2$. 51
5.2 X-ray single crystal diffraction pattern as well as heat capacity measurements of $K_xFe_{2-y}Se_2$ samples. 55
5.3 A closer look at the fundamental and superlattice peak in the $K_xFe_{2-y}Se_2$ samples. 56

6.1 Schematic plot of the Ising-like model used in the Monte Carlo simulation defined on the Fe sublattice of $K_xFe_{2-y}Se_2$. 62
6.2 Simulated structural phase transition between the Fe vacancy ordered and disordered phases of $K_xFe_{2-y}Se_2$. 64
6.3 Domain size population with different simulated quenching temperature in $K_xFe_{2-y}Se_2$. 65

List of Tables

5.1 Refined structure parameters for the *I4/m* phase of $K_xFe_{2-y}Se_2$. 57

5.2 Refined structure parameters for the *P4/mmm* phase of $K_xFe_{2-y}Se_2$. 58

Acknowledgements

First, I would like to express my deep gratitude to Professor Despina Louca, my PhD advisor, for her constructive suggestions, patient guidance, and helpful critiques during my entire PhD research at the University of Virginia. The enthusiasm she showed will always encourage me to pursue further along the road of academy.

I would like to thank all the group members: Junjie Yang, John Schneeloch, Anushika Athauda, Aaron Wegner, Zhenyang Xu, Yu Tao, and Sharon Philip. Their supports are crucial for my research.

I would like to thank Professor Gia-Wei Chern, Professor Seung-Hun Lee, and Professor Jeffrey Teo for the inspiring conversations I had with them. Many of my works would not be achieved without their generous help.

I would like to thank all the instrument scientists I worked with at Nist Center for Neutron Research, Oak Ridge National Laboratory, Los Alamos National Laboratory, and Advanced Photon Source. Data collection is fundamental to all experimental researches.

I would like to thank the Physics Department of the University of Virginia and the U.S. Department of Energy for providing founding throughout my 6 years of PhD studying.

I would also like to thank all my friends here: Tianran Chen, Depei Zhang, Sheng Gao, Xixiao Hu, Yanchu Wang, Enhao Song, Xiao Hu, Chen Cheng, Seyd Raza, Sachith Dissanayake, Anjana Samarakoon, Kapila Wijayaratne, and many others. The support, joy, and happiness they brought are unforgettable.

Finally, I would like to thank my parents, Dongsheng Duan and Yubian Ma, for their unconditional and endless support. Being abroad alone, their precious love has guided me through many difficulties in life.

Abstract

Strongly correlated materials include hosts of some of the most exciting topics in condensed matter physics, such as conventional and high-T_c superconductors, multiferroics, Mott insulators, spin/charge-density-wave materials, and topological insulators. The electron-electron correlation plays a critical role in these systems, and in many case the correlation is a result of two competing order parameters. It is therefore important to understand the interplay between the competing orders. One approach is to study the domain topology, since the competing between different long-range orders will have an impact on the spatial distribution of domains associated with each orders. The most direct experimental ways of studying domain topology are surface probes such as scanning/tunneling electron microscopes and second harmonic generation, as well as bulk probes such as focused ion beam microscope. On the other hand, neutron/X-ray scatterings, and magnetic susceptibility, transport and heat capacity measurements can give indirect information on domain topology. Both the direct and indirect data can be compared with Monte Carlo simulations to give information on the competing orders.

The electric field effect on the magnetic order in $LuMnO_3$ and the Fe vacancy order in $K_xFe_{2-y}Se_2$ are discussed in this thesis. In both projects, neutron and X-ray scattering experiments were performed to investigate the microscopic details of the system including nuclear and magnetic structures, phase volume fractions, and spin wave excitations. The information obtained from scattering was compared with simulation results using Monte Carlo method. Although the Monte Carlo models used in both projects were constructed based on lattice symmetries without microscopic details, the simulation results were still able to characterize the key features in the experiments. In $LuMnO_3$ ferroelec-

tric domain walls are coupled with the magnetic domain walls, and the external electric field has an effect on the magnetic order through the change of the domain wall distribution. In $K_xFe_{2-y}Se_2$, phase separation exists in the form of coexisting domains of the vacancy-ordered and vacancy-free phases with disordered vacancies on the domain boundaries. Post-annealing and quenching increases the volume fraction of the domain boundary as well as the Meissner shielding fraction, indicating that the vacancy disorder on these boundaries gives rise to superconductivity. In both works, the domain topology is shown to be related to the competing orders, and can be associated with novel properties such as superconductivity and the coupling between multiferroic orders.

Chapter 1

Introduction

Many materials that have played important roles in today's technologies have properties that are mostly governed by the kinetic energies of electrons and are relatively insensitive to the Coulomb repulsion between them. Metals used as building materials such as steel and aluminium, as well as semiconductors in electronics such as germanium and silicon, are good examples. The delocalized electrons in the form of Bloch waves define their mechanical, electrical, and thermal properties[1, 2]. Theories like the Fermi gas model and the nearly free electron model are quite successful in explaining the electron behaviour in these materials [1, 3, 4]. Meanwhile, there has been a growing interest among the condensed matter community in the development of the strongly correlated materials, materials with properties that cannot be explained by non- or weakly interacting electrons [5, 6]. Strong electron-electron interaction is the key feature of these systems, including the conventional superconductors with effective attraction between electrons due to electron-phonon coupling, the high T_c superconductors with unclear electron-electron interaction, charge density wave systems with the interaction between electrons and lattice distortion, magnetic materials with spin-spin couplings, and quantum spin hall systems with electrons confined in low dimensions under magnetic field [5, 6].

One very basic model for strongly correlated system is the Hubbard model [8]. The Hamiltonian consists of a hopping term **t** and an onsite Coulomb repulsion term **U**. As shown in Fig.1.1, consider a weakly interacting system with half-filled conduction band

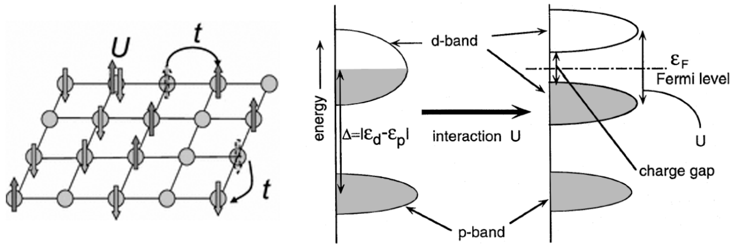

*Figure 1.1 – Schematic plots illustrating the Hubbard model and the change in band structure during Mott-insulator transition when introducing the onsite repulsive interaction **U**.[7]*

formed by d-wave electrons. If the onsite repulsion **U** is turned on, the degeneracy in d-band can be lifted. A large enough **U** can split the half-filled d-band into an empty band and a filled band with a gap in between, and drive the system from a metal to a so called Mott insulator [7, 9]. The Mott-Hubbard model can be used to explain the insulating behavior of some transition-metal oxides as well as most of the parent compounds of the cuprate superconductors in which the band theory calculation gives partially filled bands. The strength of the onsite repulsion **U** can be tuned by chemical doping, as seen in the metal-insulator transition in the Cr- and Nb-doped VO_2 and the Se-doped NiS_2 [10, 11]; or by pressure, as seen in the iron oxide Fe_2O_3 [12].

In some cases, strongly correlated materials can have more than one competing order parameter. One simple example is the J_1 J_2 Heisenberg model [13, 14, 15] with the following Hamiltonian: $H = J_1 \sum_{\langle i,j \rangle} \sigma_i \sigma_j + J_2 \sum_{\langle\langle i,j \rangle\rangle} \sigma_i \sigma_j$. As shown in Fig. 1.2, the coupling

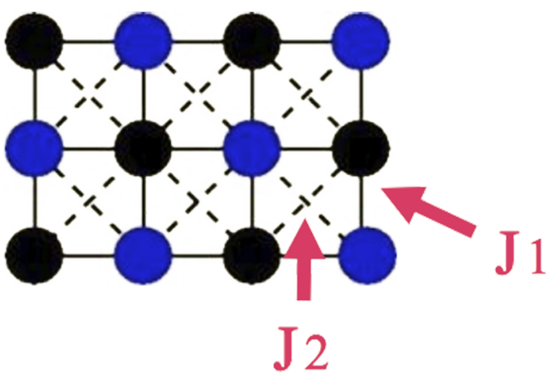

Figure 1.2 – Above shows a schematic plot of the J_1 J_2 Heisenberg model with the J_1 and J_2 interactions indicated with solid and dashed lines, respectively.[13]

constants J_1 and J_2 are defined on the first and second nearest neighbor interactions on a square lattice. When $J_2 > 0$, the second nearest neighbor antiferromagnetic interaction competes with the first nearest neighbor interaction, leading to frustration of the magnetic ground state [13]. Mean-field calculations predict a spin liquid state appearing at $|J_2|/|J_1| \sim 0.5$ [14, 15]. Materials such as Sr_2CuTeO_6 and Sr_2CWeO_6 are proposed to have J_1 J_2 like interactions dominate [16, 17, 18]. Another class of material in which competing orders are prevalent is the family of multiferroics, where two ferroic orders exist in a single phase, leading to interesting phenomena such as magnetoelectric and piezoelectric effects.

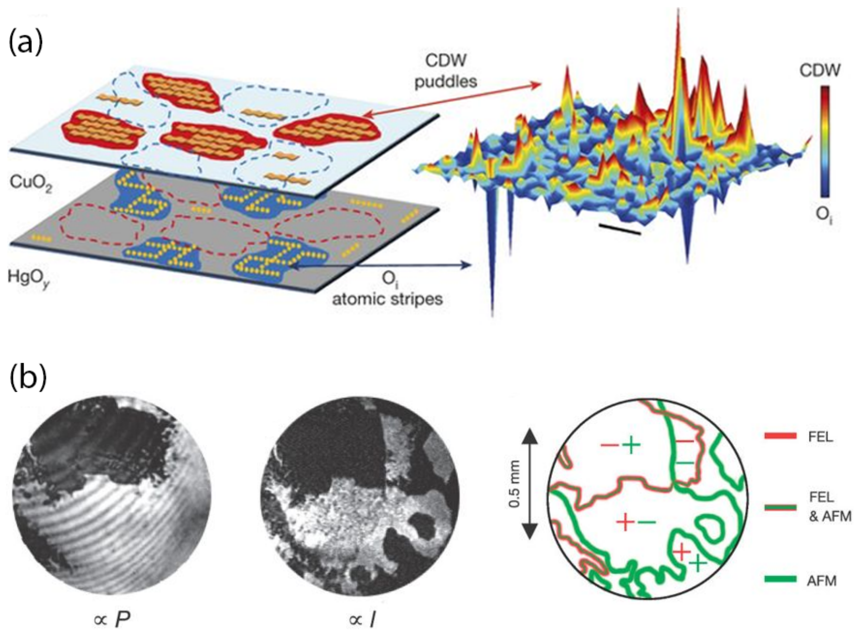

Figure 1.3 – Shown in (a) are the intensity map of the charge-density-wave and quench disorder in the CuO_2 and HgO_y layers measured by high energy X-ray diffraction [19]. Shown in (b) are the SHG study on the distribution of ferroelectric domains ($\propto P$) and antiferromagnetic domains ($\propto I$). The domain walls are plotted on a separate plot [20].

When the order parameter breaks the symmetry, domains that are related by the broken symmetry operation will be presented in the sample [1]. Factors like temperature and external field of the corresponding order (electric, magnetic, or strain field) can change the domain topology significantly [21, 22, 23]. For systems with competing orders, coupling between the order parameters can be seen in the domain walls shared by both orders

[20]. For examples, Fig. 1.3 (a) shows the domain topology of the cuprate superconductor $HgBa_2CuO_{4+y}$ observed using scanning micro X-ray diffraction [19]. An anti-correlation between the charge-density-wave puddles and the quench disorder represented by the O-rich regions is demonstrated. Fig. 1.3 (b) shows the overlap of the ferroelectric domain walls and the antiferromagnetic domain walls [20] in multiferroic $YMnO_3$. Through such domain wall coupling, it is possible to control the properties of one order parameter by turning the corresponding field of the other order.

1.1 Superconductivity

Since its discovery in 1911 [24], superconductivity has been intensively studied both experimentally and theoretically. One of the main driving force for these studies is the great application potentials of superconductors with high transition temperature T_c. For example, superconducting wires can be used for dissipationless transportation of electricity. By allowing electrons moving without resistance, extremely large magnetic field provided by extremely large current becomes feasible. Nowadays, superconducting electromagnets have already been vastly used in MRI, magnetic levitation train, and particle accelerators. Another application is in the so-called superconducting quantum interference devices (SQUIDs) where superconductors form Josephson junctions to probe magnetic field [25]. More recently, superconductors have been predicted to be a platform for quantum computing, as the superconducting vortices can trap Majorana fermions that can lead to entanglement and braiding [26, 27]. Although the superconducting transition temperature has risen to above liquid nitrogen temperature, it is still a limiting factor and an obstacle to their widespread applications. Thus, pursuing higher and higher transition temperature and the mechanism behind high T_c superconductors theoretically and experimentally has always been one of the major focus in condensed matter physics.

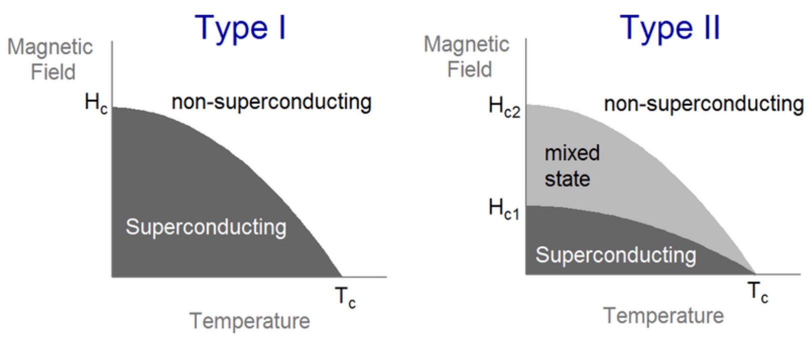

Figure 1.4 – Schematic phase diagram of type-I and type-II superconductors. The two critical magnetic fields are labeled on the type-II superconductor plot. Superconducting vortices exist in the mixed state between H_{c1} and H_{c2}.[28]

Superconductivity is a state of matter that has zero electrical resistance at very low temperature [24]. Another intrinsic feature of superconductivity is the Meissner effect, the complete screening and ejection of magnetic field upon entering the superconducting phase [29]. Superconductivity can be destroyed by finite magnetic field, and in 1935 superconductors with a second critical field that allows magnetic field to penetrate the sample through isolated points were discovered [30]. As illustrated in Fig.1.4, superconductors with one critical field are classified as type-I, and those with two critical fields are type-II.

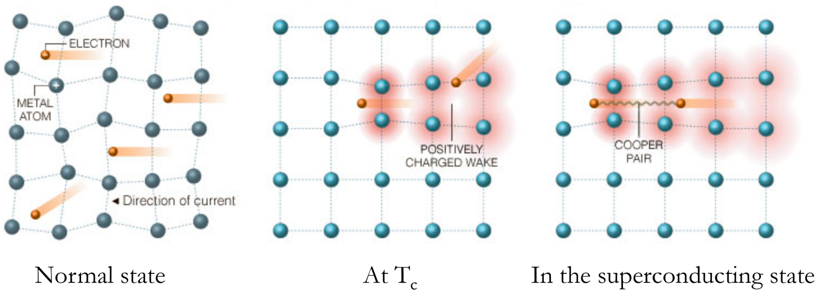

Figure 1.5 – Schematic plots illustrating the electron-phonon coupling described in the BCS theory. Phonons are shown in the form of lattice distortion.[31]

In 1950 Ginzburg and Landau brought up a mean-field theory explaining superconductivity as superfluid of electron-electron pairs formed under Bose-Einstein condensation [32]. This theory explained type-II superconductors as a result of negative free energy of the superconducting-normal state interface, which leads to partial superfluid fraction and formation of vortices where magnetic field can go through between the two critical magnetic fields [33, 34]. Later in 1957, the famous BCS theory was established, explaining the mechanism of electron-electron pairing (Cooper pairing) in conventional superconductors as the result of electron-phonon coupling [35, 36]. Figure 1.5 is a schematic plot of the electron-phonon coupling proposed in the BCS theory. The effective attraction between electrons is due to the above-background positive charge density near the lattice distortions (phonons) excited by the electrons. Group theory analysis demonstrates that any finite attraction between electrons is enough to cause Cooper pairing at finite temperature [37]. Assuming particle-hole symmetry, the normal electron band structure can be extended to electron-hole band structure, and in superconducting phase an energy gap Δ is present at the Fermi level, resulting in an energy gain of Δ for every formation of Cooper pairs [35, 36]. The energy gap starts from 0 at T_c, and saturates with a scale of $k_B T_c$ at $T \ll T_c$ [38]. BCS theory predicts $\Delta \sim 1.764 k_B T_c$ at zero temperature, and an upper limit for the superconducting temperature T_c around 30 K [39]. The whole field of superconductivity would be much less attractive if the cuprate ceramic superconductors had not been discovered to break this limit [40].

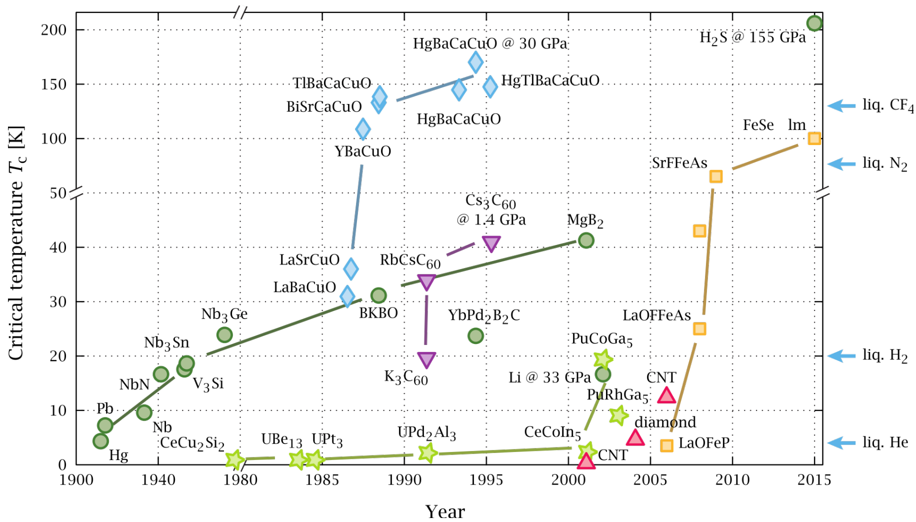

Figure 1.6 – Shown here is a timeline of the discoveries of superconductors, with BCS type marked as green circle, cuprates as blue diamond, fullerides as purple triangle, heavy fermion system as green star, and Fe-based materials as yellow square.[41]

The discovery of superconductivity in cuprates [40], followed by fulleride [42] and Fe-based compounds [43] has raised more questions than what the Ginzburg-Landau theory and BCS theory had explained. The strength of electron-phonon coupling in these materials cannot account for their higher than expected T_c, indicating different pairing mechanisms. Unlike the isotropic s-wave gap in BCS theory [35, 36], d-wave [44] or s$^{\pm}$-wave (double s-wave with opposite spins) [45] superconducting gaps were observed in these high-T_c superconductors. For the above reasons they are referred to as unconventional superconductors, as opposed to conventional superconductors where the pairing mechanism can be described by the BCS theory. After decades of intensive researches, many hypotheses have been brought out to explain these non-BCS-type pairing, including weak coupling with spin fluctuations [46] and electron/hole-pocket nesting [47, 48, 49]. But overall the theory on the unconventional superconductors is still controversial [50, 51]. Fig. 1.6 shows a timeline of the discoveries of different conventional and unconventional superconductors.

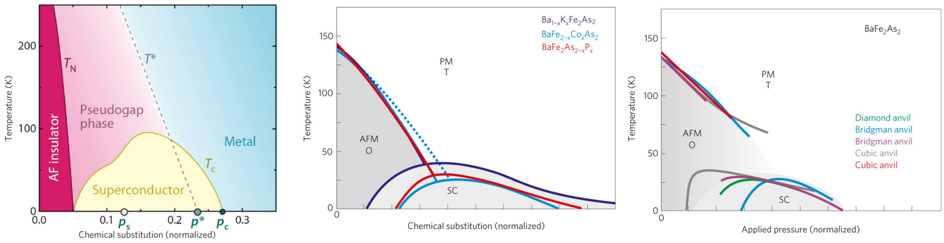

Figure 1.7 – Phase diagrams of cuprates (left) and Fe-based superconductors (middle and right). [50, 51]

Among all the unconventional superconductors, Fe-based superconductors has drawn many attentions after its discovery a decade ago [43, 51]. Historically, the notion of a competing relationship between magnetism and superconductivity had led to a tendency of avoiding magnetic elements in searching for new superconductors. Therefore the discovery of superconductivity in a system with iron, a strongly magnetic element, was totally unexpected. The Fe-based superconductors have developed into a big family including the rare earth iron pnictides RFeAsO (R = La, Nd, Sm), the alkali metal iron pnictides AFe_2As_2 (A = Ba, Sr, Ca), the alkali metal iron chalcoginides $A_xFe_{2-y}Se_2$ (A = K, Rb, Cs), as well as FeSe and FeTe thin films. The diversity and complexity in the phase diagrams of Fe-based superconductors have made this field exciting and challenging [51, 52].

Like in cuprates, the superconductivity in Fe-based materials often emerges with suppression of long-range antiferromagnetic order, as shown in Fig. 1.7 [50, 51, 52]. The difference is that the antiferromagnetic parent phases in Fe-based superconductors are not insulating as in cuprates but semimetallic [52]. As a result, for the iron pnictide family, both electron band structure calculations and angle resolved photoemission spectroscopy (ARPES) results indicate that the Fermi surfaces in these compounds consist of nearly cylindrical electron and hole pockets at the $M(\pi,0)/M(0,\pi)$ and $\Gamma(0,0)$ points, respectively [45, 53]. The high density of states from the electron and hole pockets lead to Fermi surface nesting, suggesting an $s^{\pm}$-wave pairing symmetry in the superconducting gap [45], different from the d-wave gap in cuprates [44]. On the other hand, ARPES measurements on the iron chalcoginide compounds showed different Fermi surfaces with no hole pockets at the Γ point, indicating different gap symmetries without Fermi surface nesting [54]. The Fermi surface of neither the pnictides nor the chalcoginides can be explained using the weak-coupling theory derived from cuprates, and a model with strong electron-electron correlation is needed.

Fe-based superconductors also tend to host order parameters other than antiferromagnetism prior to entering the superconducting phase. For example, the $BaFe_2As_2$ compound shows a nematic phase prior to the structural phase transition between the orthorhombic phase and the tetragonal phase [55, 56]. Here nematicity refers to the orbital of the electrons breaking 4-fold rotation symmetry of the lattice space group. Another example is the alkali metal iron chalcoginide family where a long-range order of the Fe vacancies is competing with superconductivity [57, 58, 59, 60]. The pairing mechanism in Fe-based superconductors is believed to be closely related to the spin and charge density fluctuations of these orders.

1.2 Multiferroics

Ferroics describes a large variety of systems in the field of strongly correlated materials. A phase transition separates the system into a high-temperature non-ferroic phase and a low-temperature ferroic phase. In the low temperature phase, the symmetry is lowered to allow spontaneous ordering. The most common ferroic orders are ferroelectricity [61], (anti)ferromagnetism [62], and ferroelasticity [63], as shown in Fig.1.8. Ferroelectricity is a property of materials that yields non-zero electric polarization without external electric field [61]. The space group has to be non-centrosymmetric, allowing different twin structures to have opposite polarization directions. Applying external electric field can change the polarization direction. Similarly, (anti)ferromagnetism describes spontaneous long range order of the magnetic moments [62], and ferroelasticity involves spontaneous strain in the material [63].

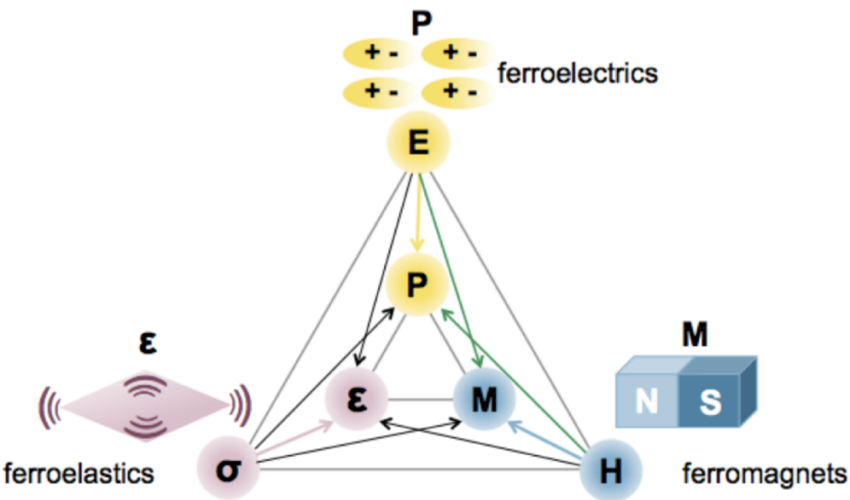

Figure 1.8 – Schematic plot illustrating the ferroic orders in multiferroic materials.

Each ferroic order on its own is enough to give rise to interesting physics and great application potentials. For example, $BaTiO_3$ is a typical ferroelectric compund with perovskite structure. At 393 K the system transits from a paraelectric cubic phase into a ferroelectric tetragonal phase with the displacement of the cations along the [001] direction with respect to the oxygen octahedrons. At 278 K, the displacement changes to the [011] direction, distorting the unit cell to an orthorhombic phase. Finally at 183 K, the displacement becomes pointing along [111] direction, resulting in a rhombohedral structure [64]. The spontanuouse polarization in this system is $0.26\ C/m^2$ and the dielectric constant is over 7000 [65]. Such high polarization and dielectric constant at room temperature have made $BaTiO_3$ extremely useful in electronic and electro-optic devices, such as thermistors, multilayer ceramic capacitors, microwave absorbers, and transducers [66].

Multiferroics are materials that host more than one ferroic order in the same phase [67, 68]. It has been a key topic of interest among the condensed matter society over the past two decades because they can serve as a great platform for magnetoelectric properties [69], such as controlling spin through electric field or controlling charge through magnetic field. If a strong coupling between the electric and magnetic orders is present around room temperature, it will have important implications on many technologies including sensors, microwave devices, energy harvesting, photo-voltaic technologies, solid-state refrigeration, data storage recording technologies, and random access multi-state memories[67].

Magnetoelectric multiferroics can be classified into type-I and type-II based on the origin of the ferroelectricity [70, 71, 72]. Ferroelectricity requires the lattice breaking inversion symmetry, which can be induced through different mechanisms including lone-pair electron activation, charge density wave, geometric rotation of the polyhedron, and magnetic order. Type-I multiferroics have different mechanisms of the magnetic and ferroelectric transitions and their transition temperatures are often well separated. Examples include perovskite materials $BiFeO_3$ [73], the thin film materials of $PbTiO_3/La_{0.67}Sr_{0.33}MnO_3$ [74], and the perovskite or hexagonal rare earth manganites $RMnO_3$ [75, 76, 77]. On the other hand, in type-II multiferroics the magnetic order is the cause of the ferroelectric order and the critical temperatures are identical. Typical type-II multiferroics include $TbMnO_3$ [70], $Ni_3V_2O_6$ [70], and $MnWO_4$ [78, 71]. Although the two ferroic orders are directly coupled, their low transition temperatures and small polarization magnitude are obstacles for their application potentials. On the other hand, type-I multiferroics have relatively high electric and magnetic transition temperatures, making them better candidates for magnetoelectric and electromagnetic devices.

Unfortunately, the presence of magnetic and ferroelectric ordering in a single phase in type-I multiferroics does not guarantee a strong coupling between them, because of the different microscopic mechanisms behind the two [67, 79, 80]. For example, in the perovskite $BiFeO_3$ and $BiMnO_3$ [73, 81], the magnetic ion Fe^{3+} and Mn^{3+} contribute to the magnetic order while the Bi^{2+} ion moves and gives rise to ferroelectricity. The different atomic origins of the two ferroic orders result in a very weak coupling, shown in the less than 0.6% dielectric anomaly under external magnetic field [80]. A more sensitive dielectric anomaly controlled by magnetic field was observed in the so-called "frustrated magnets", including the perovskite and hexagonal manganites $RMnO_3$ and RMn_2O_5 [75, 76, 77], $MnWO_4$ [78, 71], and $Ni_3V_2O_8$ [82]. These materials have degenerated magnetic ground states due to geometrical frustration of the magnetic ion sublattice. The magnetoelectric coupling in these systems is likely due to the correlation of both magnetic and electric orders with the lattice geometry.

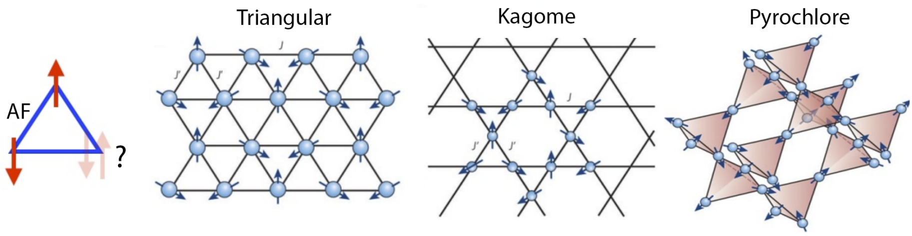

Figure 1.9 – Schematic plot illustrating the geometrical frustration in trangular, kagome and pyrochlore lattices. [83]

In frustrated magnets, spins cannot be aligned in a Néel order [83]. The complexity in spin structures and the surrounding superexchange paths lead to single-ion anisotropy and Dzyaloshinskii–Moriya interaction (DMI) [84, 85]. The corresponding Hamiltonian for DMI has the following form: $H_{DM} = D_{i,j} \cdot (\boldsymbol{S_i} \times \boldsymbol{S_j})$. When dominant, the DMI can give rise to chiral magnetic orders or excitations (Skyrmions) [86, 87]. When competing with the Heisenberg term $H = J_{i,j}\boldsymbol{S_i} \cdot \boldsymbol{S_j}$, the DMI can lead to a magnetic induced lattice relaxation and a weak coupling between the magnetic and electric orders [88, 89].

The layout of this thesis is the following. In chapter 2, two main research techniques involved in this thesis, neutron/x-ray scattering and Monte Carlo simulation, are discussed. In chapter 3 the experimental studies on the multiferroic $LuMnO_3$ under external electric field using neutron scattering are shown [90]. In chapter 4 the Monte Carlo simulations of the two competing orders in $LuMnO_3$ are discussed [90]. In chapter 5, experimental results on the Fe vacancy ordering in Fe-based superconductor $K_xFe_{2-y}Se_2$ are presented [55, 91]. In chapter 6, Monte Carlo simulation results on the Fe sublattice of $K_xFe_{2-y}Se_2$ are demonstrated [91, 92]. Chapter 7 is the discussion, and chapter 8 is the conclusion of the thesis.

Chapter 2

Methods

2.1 X-ray/Neutron Scattering

Both X ray and neutron can be used in scattering experiments to investigate microscopic details of the static and dynamic crystal structures of matters [93]. In elastic scattering channel, the diffraction pattern formed by scattering off a crystalline sample is a convolution of the Fourier transform of real space information with a profile function. In the inelastic channel, scattered intensities at non-zero transferred energy ΔE represent different dynamic modes excited by the incident beam. With proper analysis, scattering data can help determining the crystal structure, magnetic structure, local lattice distortions, phonon density of states, spin wave spectrum and other important properties.

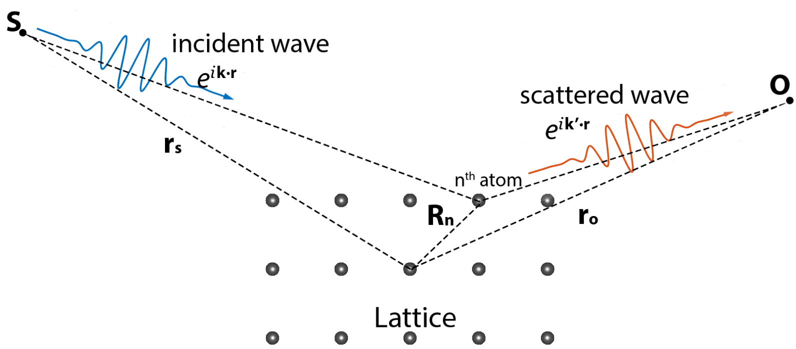

Figure 2.1 – Schematic plot of plane wave scattering off from a simple cubic lattice.

As illustrated in Fig. 2.1, if assuming incident beam of neutron or x-ray is a plane wave with amplitude $A \propto \mathrm{e}^{\mathrm{i}2\pi\boldsymbol{k}\cdot\boldsymbol{r}}$, the scattered wave from a simple cubic lattice with one atom per unit cell at observing point O has the following form:

$$A(\boldsymbol{k},\boldsymbol{k}') \propto \sum_{\boldsymbol{R_n}} \mathrm{e}^{\mathrm{i}2\pi\boldsymbol{k}(\boldsymbol{r_s}+\boldsymbol{R_n})}\mathrm{e}^{\mathrm{i}2\pi\boldsymbol{k}'(\boldsymbol{r_o}-\boldsymbol{R_n})} \propto \sum_{\boldsymbol{R_n}} \mathrm{e}^{\mathrm{i}2\pi(\boldsymbol{k}-\boldsymbol{k}')\boldsymbol{R_n}} \tag{2.1}$$

Here $\boldsymbol{k}$ and $\boldsymbol{k}'$ are the wave vector of the incident and scattered beam, $\boldsymbol{R_n}$ represents the position vector of the nth unit cell in the lattice. $\boldsymbol{r_s}$ and $\boldsymbol{r_o}$ are the vector of the source and the observing point relative to the sample, respectively. The vector $\boldsymbol{R_n}$ is the real space position vector of the nth unit cell, and can be written as a combination of the lattice primitive vectors $\boldsymbol{a_1}$, $\boldsymbol{a_2}$ and $\boldsymbol{a_3}$ with integer coefficients: $\boldsymbol{R_n} = n_1\boldsymbol{a_1} + n_2\boldsymbol{a_2} + n_3\boldsymbol{a_3}$. And the vector $\boldsymbol{\kappa} \equiv \boldsymbol{k} - \boldsymbol{k'}$ can be written as combination of the reciprocal unit vectors $\boldsymbol{b_1}$, $\boldsymbol{b_2}$ and $\boldsymbol{b_3}$: $\boldsymbol{\kappa} = \kappa_1 \boldsymbol{b_1} + \kappa_2 \boldsymbol{b_2} + \kappa_3 \boldsymbol{b_3}$, where $\kappa_i \in R$. From the orthonormality of the primitive and reciprocal unit vectors $\boldsymbol{a_i} \cdot \boldsymbol{b_j} = \delta_{ij}$, The sum in Eq. 2.1 becomes:

$$\prod_{i=1,2,3} \sum_{n_i=1}^{N_i} \mathrm{e}^{\mathrm{i}2\pi\kappa_\mathrm{i}\mathrm{n}_\mathrm{i}} = \prod_{\mathrm{i}=1,2,3} \varphi(\mathrm{N_i}) \frac{\sin(\pi\kappa_\mathrm{i}\mathrm{N_i})}{\sin(\pi\kappa_\mathrm{i})} \tag{2.2}$$

Here N_i represents the number of unit cells along the $\boldsymbol{a_i}$ direction. Since N_i has the scale of Avogadro constant, the sum goes to zero for any non-integer value of κ_i, and gives $N = N_1 N_2 N_3$ for integer values. With that, Eq. 2.1 gives the Bragg's law:

$$A(\boldsymbol{k}, \boldsymbol{k'}) \propto N \sum_{h,k,l \in Z} \delta(\boldsymbol{\kappa} - \boldsymbol{G}_{hkl}) \tag{2.3}$$

The scattered beam has intensity only when $\boldsymbol{\kappa} = \boldsymbol{G}_{hkl}$ with the reciprocal vector $\boldsymbol{G}_{hkl} = h\boldsymbol{b_1} + k\boldsymbol{b_2} + l\boldsymbol{b_3}$. Each set of Miller indices h, k, l corresponds to a series of crystal planes in the lattice with a d-spacing $d_{hkl} = 2\pi/|G_{hkl}|$. In the case of elastic scattering, $|\boldsymbol{k}| = |\boldsymbol{k'}|$, Eq. 2.3 can be written in a more familiar form in terms of d-spacing, scattering angle 2θ, and incident wavelength λ:

$$n\lambda = 2d \sin\theta. \tag{2.4}$$

Bragg's law determines the position of the reflected beam, while the intensity of these reflection depends on the form factor and the structure factor. The structure factor is related to the space group of the unit cell, the site symmetry of each atoms, the Miller indices of the Bragg reflection, and the form factor of each atoms at the given $\boldsymbol{G}_{hkl}$. The form factor characterizes the interaction between the incident beam and the sample, and depends on the type of incoming wave as well as the type of atoms. For x ray, the scattering is due to electromagnetic interaction with the electron clouds surrounding the atoms, and the x-ray form factor is the Fourier transform of the electron density. For neutron, the scattering consists of two parts: one is the strong interaction between the neutron and the nuclei of the atoms, and the other is the electromagnetic interaction between the spin of neutron and the magnetic moment in the lattice. The nuclear part is represented by pseudo potential and scattering length, while the magnetic part is proportional to the ordered moment.

The major difference between neutron and x ray in scattering experiment lies in the form factor. The total integration of x-ray form factor is proportional to the number of electrons in the atom, thus x ray does not scatter well off light elements such as H and Li. It also lacks the ability to probe magnetic orders in the lattice. The neutron scattering length does not scale with the atomic number and is rather random from one type of atom to another. It can interact with magnetic moment of the atom and help determine magnetic orders or excitations. Another advantage of neutron scattering comes from the fact that neutrons are not relativistic particles and have different velocities for different wavelengths. The time of flight of neutrons carries information of their energy, allowing the energy and momentum space coverage to be enhanced by using white beam. On the other hand, X ray is relatively easier to acquire comparing to neutron. An in-house X-ray diffractometer can provide enough information for structure determination, while a synchrotron light source can generate x ray with tunable wavelength and much higher flux. Neutron sources with the suitable wavelength and flux for scattering experiment require either a research nuclear reactor or a spallation facility. And even for the most powerful ones, the fluxes are still orders of magnitude lower than those of synchrotron x-ray sources.

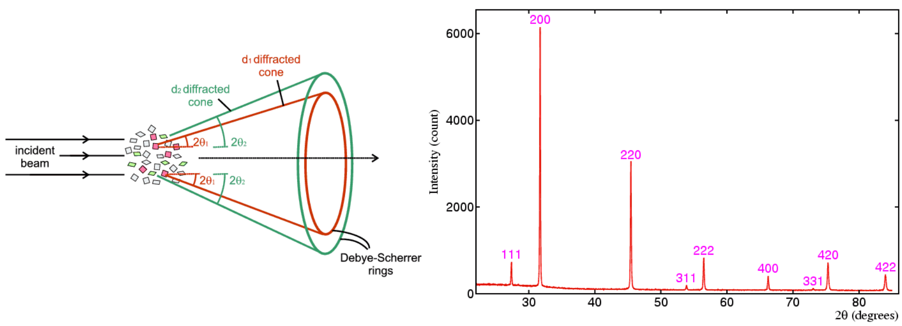

Figure 2.2 – Shown in the figures are a schematic plot of powder diffraction (left) and a typical powder diffraction pattern of NaCl (right). [94]

The crystalline sample used in scattering experiment can be in powder form or single crystal form. For powder scattering, because each small grain of the sample has its own orientation, the angular degrees of freedom will be integrated out, and the collected data become a function of the momentum transfer magnitude $|\boldsymbol{G}_{hkl}|$, as shown in Fig. 2.2. Such a powder scattering experiment does not require any form of alignment of the sample at a cost of losing the angular degree-of-freedom information. A method called Rietveld refinement is specialized in solving the static crystal structure from powder data [95]. In Rietveld refinement, structure factors of each Bragg reflections are calculated based on an initial crystal structure, and are convoluted with profile functions to reproduce the one dimensional powder histogram. Parameters like the scaling factors, lattice constants, atom coordinates, occupation numbers, and thermal factors are fitted with the data using least-square method. Once the parameters are optimized, the refinement result becomes a possible solution of the average crystal structure. Powder diffraction data can also be analysed through pair distribution function, which requires high resolution and large coverage in the momentum space, and can provide information on the local structure.

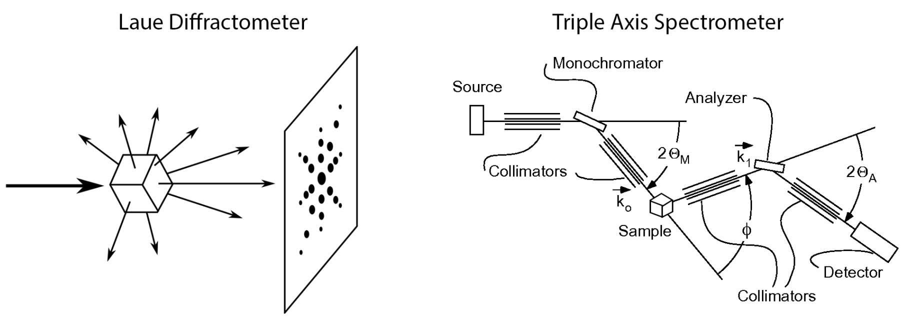

Figure 2.3 – Schematic plot of Laue diffractometer (left) and triple axis spectrometer (right). [94]

When single crystal samples are used, more information such as diffuse scattering, anisotropic strain or twinning ratio can be obtained, at a cost of relatively small momentum space coverage and slow data collecting rate. Such experiments include Laue diffraction, triple-axis diffraction, and four-circle diffraction, as shown in Fig. 2.3. In Laue diffractometer, incident beam is focused at the sample to create diffraction peaks with different momentum transfer $\boldsymbol{G}_{hkl}$. A 2D detector is placed either in front or behind the sample, and the collected data show the so called Laue pattern. Laue diffraction does not measure the energy of the scattered beam, thus does not provide energy resolution. To survey the energy transfer channel with single crystal, the neutron triple axis spectrometer comes into use. On the right panel of Fig. 2.3 is a schematic plot of a triple axis spectrometer. A certain wavelength of the incident beam is selected by the monochromator before hitting the sample. An analyzer is placed at an angle with respect to the incident beam to pick up the wanted outgoing wavelength. "Triple axis" refers to the three adjustable axes in the instrument that are perpendicular to the sketched plane: the axis passing through monochromator, the axis around which the sample can rotate, and the axis of the analyzer. This setup allows measuring the intensity of the reflected beam with energy different from the incident energy, providing access to the inelastic channel. with the help of time-of-flight technology, neutron scattering spectrometers with 2D area detectors are feasible, allowing a much faster data collection speed. To resolve the angular degree-of-freedom, one has to either align the sample with a goniometer before taking the data or construct an orientation matrix in reciprocal space after taking the data. Both methods require high quality single crystal samples.

2.2 Monte Carlo Simulation

In condensed matter physics, most many-body Hamiltonians are not analytically solvable. The test and proof of such theories and models then relies on certain mathematical/computational methods, such as the mean-field approximation, the density functional theory, and the Monte Carlo method.

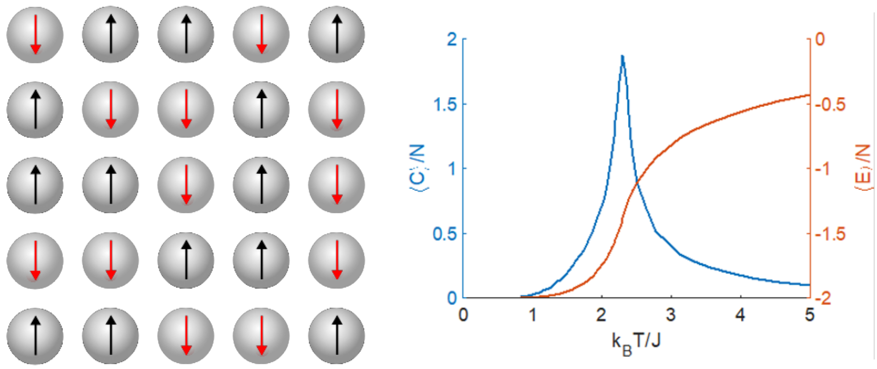

Figure 2.4 – Shown here are a schematic plot illustrating 2D Ising model (left) and the corresponding simulation results showing magnetic phase transition (right).

Monte Carlo method is a computational technique that can simulate a probability distribution with the help of random sampling. An early example of random sampling is the Buffon's needle experiment [96], where needles are dropped randomly on parallel lines to estimate the value of π. In Monte Carlo simulation, large enough amounts of pseudo random numbers are generated to simulate certain probability distributions. Since many-body system can be described using statistical ensembles, one can then simulate a many-body problem by random samplers that follow the probability distribution defined by the corresponding ensemble. One example is the Monte Carlo simulation of the 2D and 3D Ising model [97]. Ising model describes a lattice consists of spin 1/2 particles with nearest neighbor Heisenberg interaction, as shown in Fig. 2.4. The Hamiltonian is $H = -\sum_{\langle i,j \rangle} J\sigma_i\sigma_j$ with $\sigma_i = \pm 1$ represents the spin 1/2 degree-of-freedom on the ith site, J represents the nearest neighbor coupling strength, and the sum goes through all pairs of nearest neighbors $\langle i,j \rangle$. On the simulated lattice, a random change on the spin configuration is proposed in a way that satisfies the detailed balance rule and is accepted with a probability of $\mathrm{e}^{-\beta \Delta \mathrm{E}}$. Here ΔE is the energy difference between the new spin configuration and the old one, and $\beta \equiv 1/k_B T$ is the reciprocal of the thermodynamic temperature. With enough number of iterations, the simulated spin configuration will be stabilized in a state that minimizes the free energy. By achieving such thermodynamic equilibrium at different temperatures, the properties of the magnetic phase transition can be captured. In the simulation process, properties such as total energy E and magnetic order parameter m can be calculated at each spin configuration. If two spin configurations are separated by enough number of iterations, the two states can be considered independent. Averaging over many independent states at a given temperature makes the statistical averages $\langle E \rangle$ and $\langle m \rangle$ good representatives of the corresponding bulk properties of the simulated lattice at that temperature. Combining with $\langle E^2 \rangle$ and $\langle m^2 \rangle$, the heat capacity C and magnetic susceptibility χ are also represented. The accuracy of these statistical estimates increases with the sampling size, and the scaling speed depends on the type of Monte Carlo algorithm.

As shown in the right panel of Fig. 2.4, the magnetic phase transition in 2D Ising model is captured by a Markov chain Monte Carlo simulation. With different choices of the simulated lattice size L, the measured quantities E, m, C, and χ will develop different temperature dependent curves. A method called finite size scaling can be used to determine the critical exponents of the phase transition by re-scaling the temperature and the measured quantities with the size L until each curve overlaps with each other. A typical finite size scaling analysis on the 2D Ising model is shown in Fig. 2.5, where the 4th order Binder's cumulant B_4, heat capacity C, magnetization m, and magnetic susceptibility χ are sampled and scaled with different lattice size L to obtain the critical exponents: $\nu = 1$, $\beta = 1/8$, $\gamma = 7/4$. By comparing the simulated results of the critical exponents with theory predictions, one can determine the universality class of the phase transition.

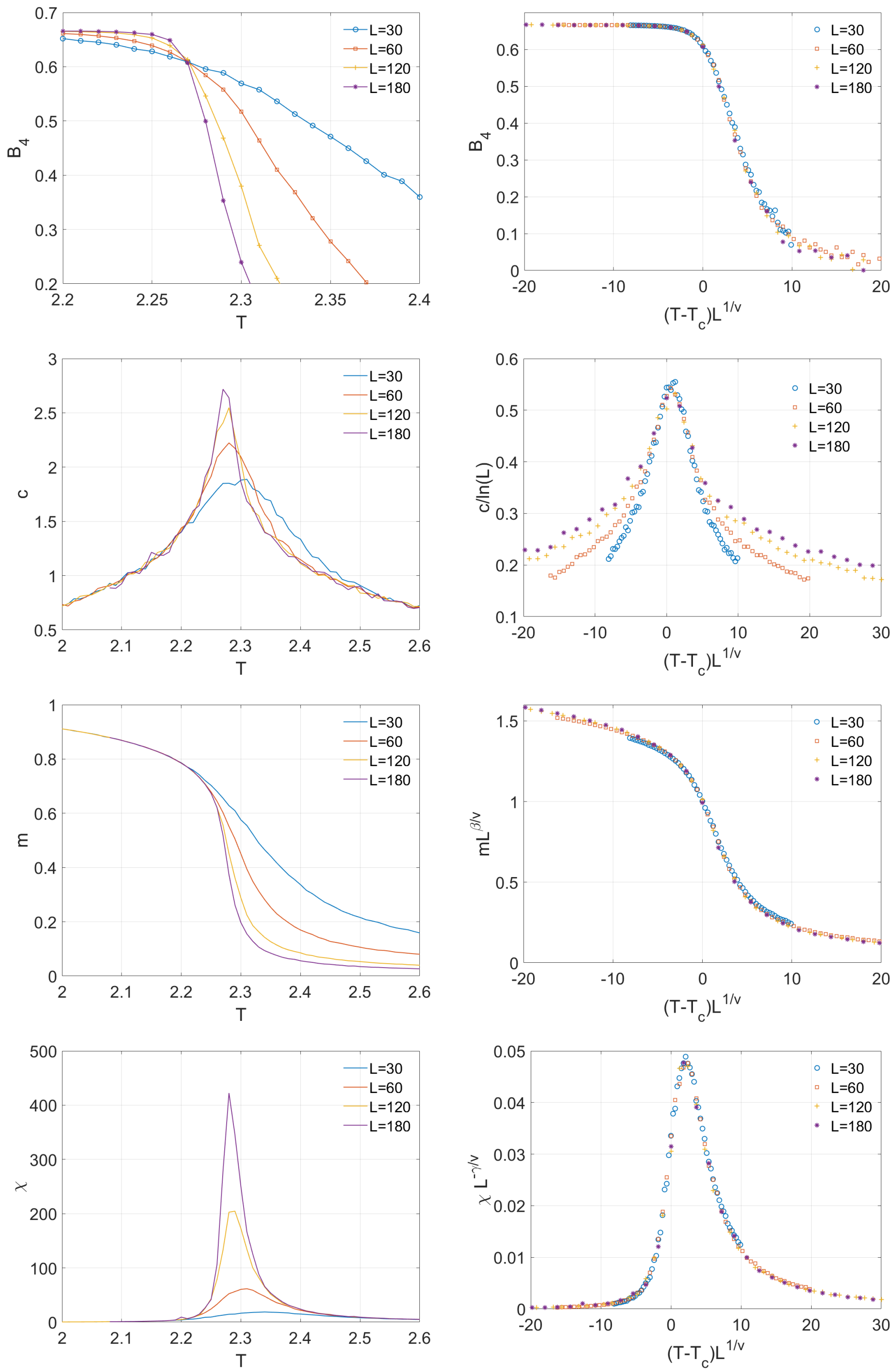

Figure 2.5 – Shown here are the finite size scaling results on the Monte Carlo results of 2D Ising model. On the left panel are the data versus temperature as collected. On the right panel are the scaled data. The 4^{th} order Binder's cumulant B_4 is used to determine the transition temperature.

Chapter 3

Neutron Scattering Study on the Coupling of Magnetism and Ferroelectricity in the Hexagonal Multiferroic $RMnO_3$

3.1 Introduction

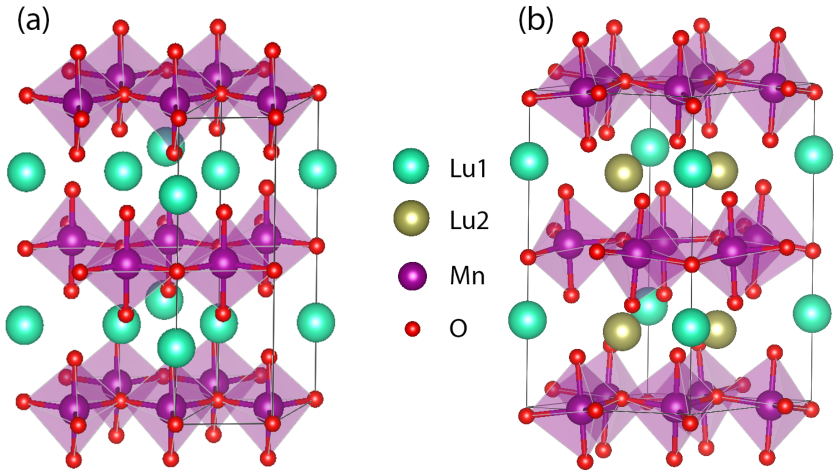

Figure 3.1 – Shown in (a) and (b) are the crystal structures of $RMnO_3$ above and below the ferroelectric transition temperature T_C, respectively. The arrow in (b) indicates the direction of the MnO_5 bipyramid tilting (a.k.a. trimerization).

As a typical type-I multiferroics, the hexagonal $RMnO_3$ (R = Y, Lu, Sc,$\cdots$) becomes ferroelectric below $T_C \sim$ 570-990 K when the crystal transits from the high temperature *$P6_3mmc$* phase to the low temperature *$P6_3cm$* phase through a structural instability of the Mn and O atoms due to trimerization [75, 76, 77]. The trimerization then leads to the rare earth atom splitting into two atomic sites which breaks inversion symmetry and gives rise to polarization, as illustrated in Fig 4.1 (b). The polarization coming from such small lattice distortion is an order of magnitude smaller than a regular ferroelectric material [98, 99]. Since the Mn atoms form triangular lattice in the ab plane, the system becomes geometrically frustrated [100]. Below $T_N \sim 90$ K, the magnetic moment of Mn orders in a 120° arrangement [101, 102, 103]. Based on representation analysis, 4 possible magnetic structures ($\Gamma1$, $\Gamma2$, $\Gamma3$, and $\Gamma4$) with maximum magnetic group symmetry are shown in Fig. 3.2 [102]. In magnetic structures $\Gamma1$ and $\Gamma4$, the moments of Mn atoms are aligned in the ab plane perpendicular to the center of the trimerization, whereas in $\Gamma2$ and $\Gamma3$ the moments are canted out-of-plane and pointed towards or away from the trimerization center.

With only Heisenberg interactions, the magnetic ground states are degenerated as

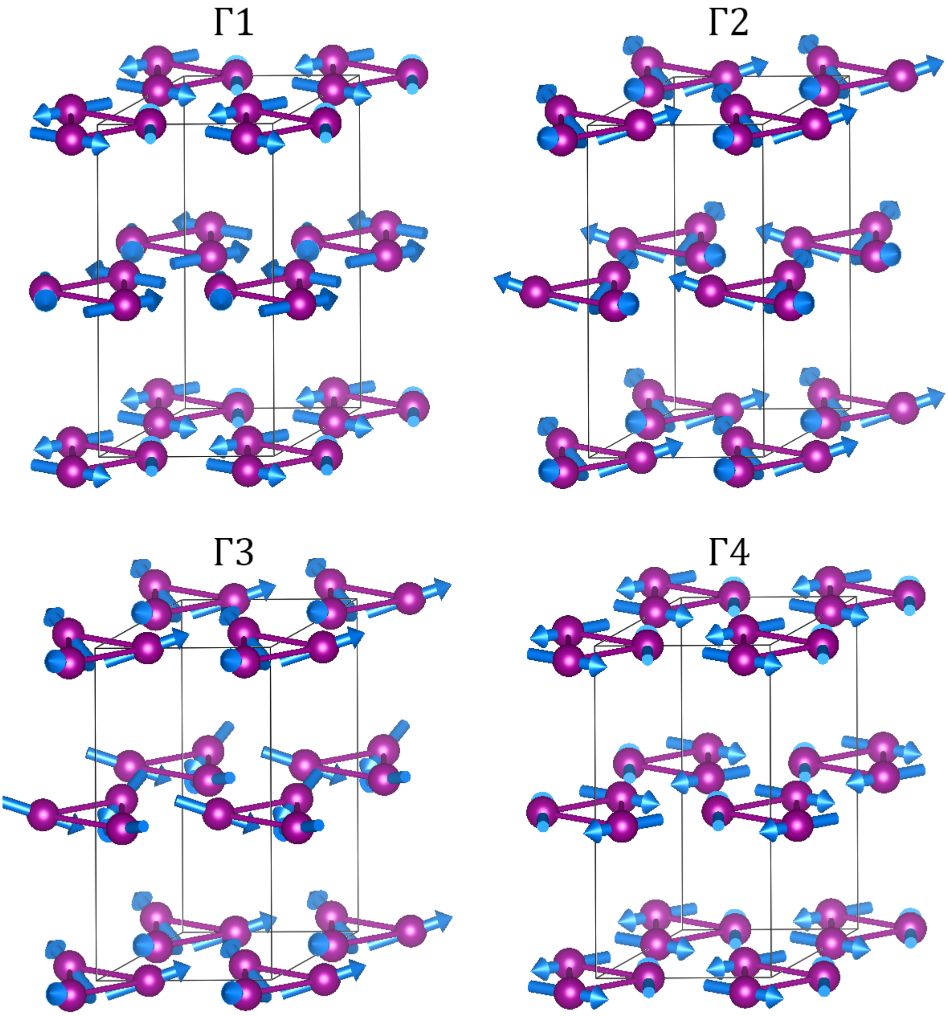

Figure 3.2 – According to representation analysis, 4 possible magnetic structures of hexagonal $RMnO_3$ with highest magnetic subgroup are plotted and label as $\Gamma1$-$\Gamma4$. Only Mn sublattice is plotted. The purple bonds between Mn atoms indicate the trimerization unit, and the blue arrows represent the magnetic moment.

long as a 120° spin configuration is satisfied. The spin-orbit coupling introduces in-plane anisotropy and lifts the degeneracy [104]. The out-of-plane canting is likely due to the antisymmetric terms in the Hamiltonian, the Dzyaloshinskii–Moriya interaction [89, 105]. Different choice of the rare earth element results in different coupling strengths for the in-plane and out-of-plane anisotropies, leading to different magnetic ground state. For example, *ab initio* calculations on $YMnO_3$ and $LuMnO_3$ suggest $\Gamma3$ and $\Gamma4$ as the magnetic ground state, respectively [104]. In a similar compound, $Lu_{0.5}Sc_{0.5}FeO_3$, the system goes through two magnetic transitions from the $\Gamma2$ structure to an indistinguishable $\Gamma1$ or $\Gamma3$ structure [103]. Polarized neutron scattering can provide additional information about the out-of-plane spin arrangement to distinguish between $\Gamma1$ and $\Gamma3$, and between $\Gamma2$ or $\Gamma4$. Whereas the difference between the two groups: $\Gamma1/\Gamma3$ and $\Gamma2/\Gamma4$ can be determined using the magnetic peak (100) which only presents in the former.

The weak interaction between magnetism and ferroelectricity in $RMnO_3$ has been observed through in-plane dielectric anomaly with external magnetic field [106]. It is then very natural to ask if an external electric field can have any effect on the magnetic order in this system. To find out, single crystal neutron scattering experiments were performed on $LuMnO_3$ [90].

3.2 Neutron Scattering Results

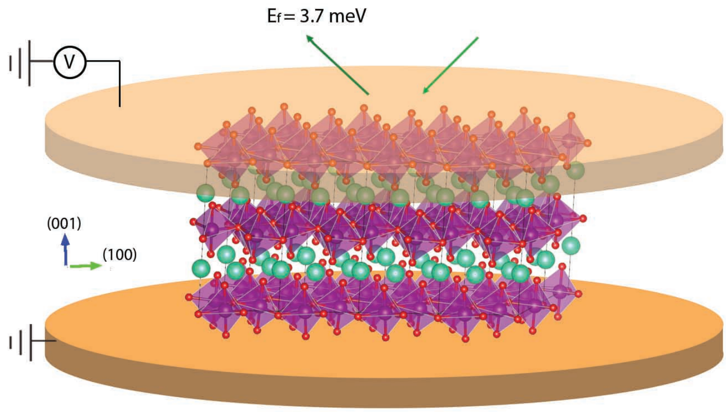

Figure 3.3 – Shown above is a schematic plot showing the experimental setup. The (001)-cut single crystal $LuMnO_3$ sample was glued between two Al plates by silver paint. The Al plates served as parallel plate capaciter and provided static electric field across the sample.

The neutron scattering experiments were performed on the triple axis spectrometer SPINS at Nist Center for Neutron Research. External electric field was applied on the sample along c direction. The experiment setup is shown in Fig. 3.3. Two aluminium plates were glued on the two sides of a (001)-cut single crystal sample using silver paint, serving as a parallel plate capacitor to provide static electric field on the sample. One single crystal sample was cut into two pieces, so electric field of opposite direction can be applied on the same sample from its unpolarized state.

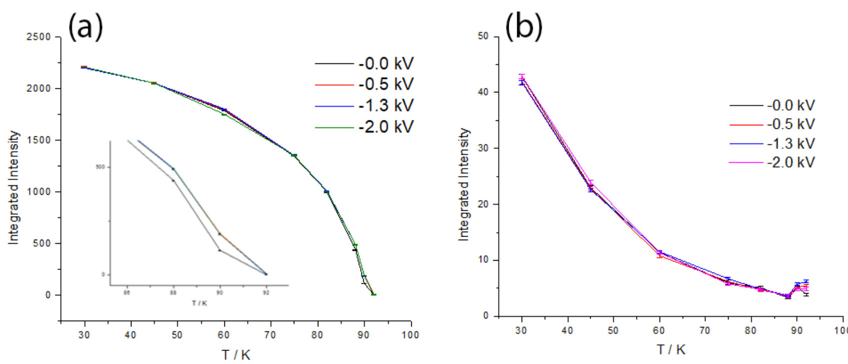

Figure 3.4 – Shown in (a) and (b) are magnetic order parameter plots of $LuMnO_3$ extracted from the intensity of (101) and (100) peaks, respectively. The inset in (a) is a zoomed-in plot of the (101) intensity at the vicinity of the transition temperature $T_N \sim 90\ K$.

Shown in Figs. 3.4 (a) and (b) are the integrated intensities of magnetic peaks (101) and (100) as functions of temperature, respectively. A typical order parameter curve was observed in the magnetic peak (101), in agreement with the calculated magnetic ground state Γ_4. The magnetic peak (100) is absent in the Γ_4 structure, and the weak intensity observed in our sample was likely due to nuclear contribution of the trimerized lattice.Shown in Fig. 3.5 is the scan along L direction across the magnetic peak (101) under different electric field near the magnetic phase transition. Starting from the fresh (unpolarized) state,

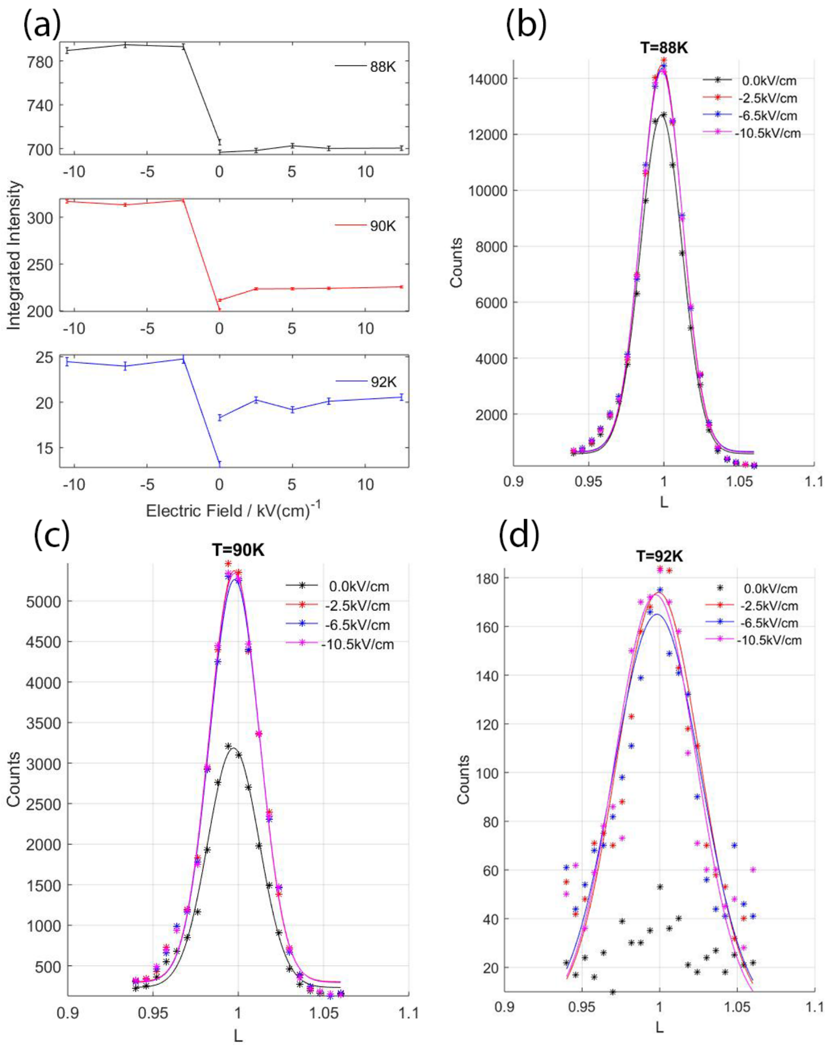

Figure 3.5 – Shown above are the elastic neutron diffraction data. Scans along L-direction through the magnetic peak (101) were performed under different electric field at the vicinity of the magnetic phase transition temperature T_N=92 K. Subplot (a) gives the integrated intensities of the magnetic peak (101) as a function of electric field.

the sample showed an enchancement of the (101) peak intensity when applying negative E-field, and remained unaffected when applying positive E-field. Due to the large coercive field of this compound, such field effect on the magnetic peak were not reversible under our setup with a maximum field of 15 kV/cm limited by the power supply and the sample thickness.

Inelastic neutron scattering were also observed near the (100) magnetic peak, as shown in Fig. 3.6. The excitation at 0.4 meV comes from the single-ion anisotropy (SIA) in the system. The calculated spin wave spectrum is shown in Fig. 3.6. The position and intensity of this SIA gap did not show a significant electric field dependence, suggesting that the effect of external electric field on the magnetic order is not applied through the single-ion anisotropy.

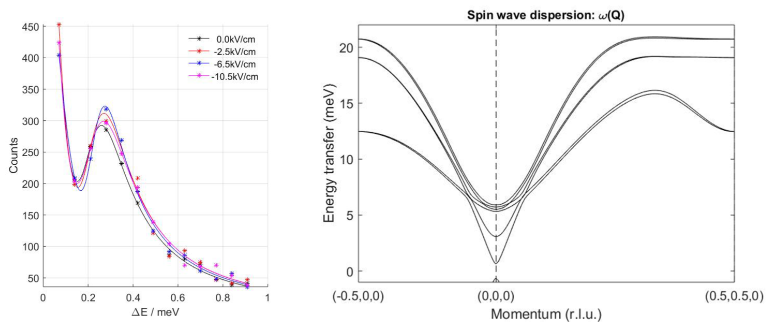

Figure 3.6 – Shown on the left are the inelastic neutron diffraction data. Scans along ΔE at the magnetic peak (100) were performed under different electric field at T=90 K. Shown on the right is a calculated spin wave spectrum with single ion anisotropy on Mn atoms.

3.3 Summary

Neutron scattering experiments on single crystal $LuMnO_3$ showed a magnetic ground state of $\Gamma 2/\Gamma 4$ setting in at $T_N \sim 90\ K$, while the iconic peak (100) of the $\Gamma 1/\Gamma 3$ structure demonstrated a different temperature dependence. Inelastic scattering at (100) peak position revealed a spin wave excitation with the excitation energy ΔE. The energy gap calculated at the Γ point on the spin wave spectrum suggested that the excitation is related to single ion anisotropy. The intensity of (100) peak might be a result of the lattice trimerization which also leads to single ion anisotropy. Under external electric field of certain direction, the magnetic peak (101) showed an enhancement near T_N, indicating the existence of a electric field controlled change on the magnetic order.

Chapter 4

Monte Carlo Simulation on the Coupling of Magnetism and Ferroelectricity in the Hexagonal Multiferroic $RMnO_3$

4.1 Introduction

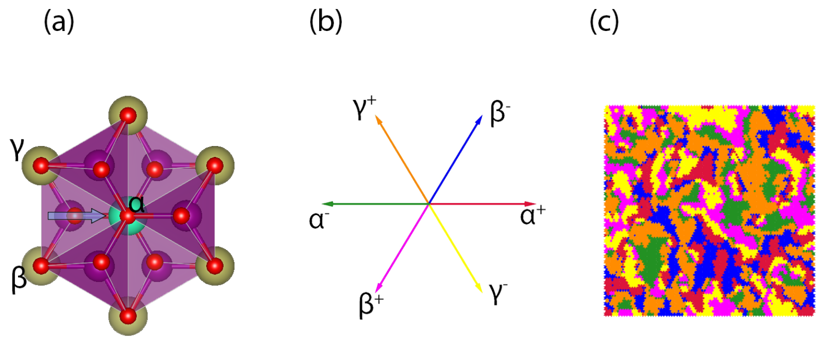

Figure 4.1 – Shown in (a) and (b) are the crystal structures of $RMnO_3$ above and below the ferroelectric transition temperature T_C, respectively. The arrow in (b) indicates the direction of the MnO_5 bipyramid tilting (a.k.a. trimerization). In (c) shows the 6 symmetry equivalent trimerization directions, which correspond to the 6 structural domians as labeled in (d). Shown in (e) is a typical simulated lattice below T_C.

The ferroelectric phase transition in $RMnO_3$ consists of the MnO_5 bipyramid tilting (trimerization) and the rare earth site splitting. The former breaks the Z_3 symmetry of the high temperature $P6_3mmc$ phase [75, 76, 77] while the latter breaks the Z_2 symmetry and gives rise to polarization. Such a $Z_3 \times Z_2$ symmetry breaking creates 6 structural domains. As shown in Figs.3.1 (a), (b) and Fig. 4.1 (a), the corner sharing MnO_5 bipyramid layers are separated by the rare earth atom layers. From the top view, each MnO_5 bipyramid is surrounded by 3 Lu atoms (α,β,γ). The trimerization involves tilting of the bipyramids towards one of the 6 symmetry equivalent directions: α^+,β^+,γ^+,α^-,β^-,γ^-, each of which corresponds to a structural domain [76]. This has been confirmed by observations using optics second harmonic generation, SEM, STM and AFM [20, 76, 107, 108, 109, 110]. On top of the ferroelectric order there is the magnetic order which can be characterized by Heisenberg interactions, single ion anisotropies, and Dzyaloshinskii–Moriya interactions [89, 105].

The coupling between the magnetic and electric orders in a type-I multiferroic system is usually weak [68, 67]. In the hexagonal rare earth manganite system, the microscopic origins of such a weak coupling lies in the correlation of the lattice trimerization with both magnetic and electric orders [20]. On one hand, the electric polarization is a direct result of the bipyramid tilting and rare earth site splitting. On the other hand, the center of trimerization defines the center of the single ion anisotropy terms for the magnetic orders. As a result, a ferroelectric domain wall simultaneously serves as an antiferromagnetic domain wall, giving rise to a weak coupling between the two ferroic orders.

4.2 Monte Carlo Simulation

To further study such a weak coupling through domain walls, Monte Carlo simulations on the ferroelectric order and magnetic order of $RMnO_3$ were performed. The nearest neighbor coupling of both order parameters are confined in the xy-plane due to the crystal geometry [111]. For ferroelectric order, a 2D 6-fold clock model without microscopical details was used [112]. For magnetic order, an x-y model with Heisenberg interactions and single ion anisotropy terms was employed. The Dzyaloshinskii–Moriya interaction was neglected since it mainly gives rise to the out-of-plane canting, which is a minor fraction of the total ordered magnetic moment in this system [102, 104].

The ferroelectric part of the Hamiltonian has the following form:

$$H_E = -\sum_i A_E \cos(6\varphi_i) - \sum_{\langle i,j \rangle} J_E \cos(\varphi_i - \varphi_j) \tag{4.1}$$

Here φ_i represents direction of the bipyramid tilting on the ith unit cell, A_E is the structural anisotropy coefficient, and J_E is the coupling constant between the nearest neighbor $\langle i, j \rangle$. To simulate the hexagonal crystal structure of $RMnO_3$, the Hamiltonian is defined on a triangular lattice. The first term determines 6 minima of the simulated variable: $\varphi_n = \frac{n\pi}{3}$ with $n = 0, 1, \cdots 5$, each corresponding to one of the 6 structural domains, as illustrated in Fig.4.1 (d). The second term introduces ferroelectric coupling between nearest neighbors with positive value of J_E. The Metropolis Monte-Carlo algorithm is used to simulate the system. In each iteration, a unit cell i is chosen randomly. A random change $d\varphi$ is proposed to be added on φ_i, and will be accepted with probability $MIN(1, \exp(-\beta\Delta E))$, with ΔE being the corresponding change of the total energy and $\beta = \frac{1}{k_B T}$. A typical simulated lattice in the ferroelectric phase is shown in Fig.4.1 (e), where different domains are painted in different colors. The domain walls always cross at the junctions of all 6 domains, forming Z_6 vortices, which are direct results of the $Z_3 \times Z_2$ symmetry breaking. In the simulation the vortices always appear in two low-energy cyclic sequences: $\alpha^+, \beta^-, \gamma^+, \alpha^-, \beta^+, \gamma^-$ and $\alpha^+, \gamma^-, \beta^+, \alpha^-, \gamma^+, \beta^-$, in agreement with the experimental observations [108, 109, 110]. In 3D the vortices in each xy-plane are connected, forming vortex loops [112, 111].

The order parameter of this Z_6 symmetry breaking transition is defined as:

$$m_{Z_6} = \frac{1}{N}\left\{\left[\sum_i \cos(\varphi_i)\right]^2 + \left[\sum_i \sin(\varphi_i)\right]^2\right\}^{1/2} \tag{4.2}$$

If the variable φ goes through 2π or -2π across the 6 nearest neighbors of a site i, this site is classified as a vortex with positive or negative cyclic sequence. With this definition, the high temperature phase consists of high density of vortices. The polarization per site of the simulated lattice is calculated by:

$$P = p_0 \sum_i \cos(3\varphi_i)/N \tag{4.3}$$

Here P_0 is the unit dipole moment of a unit cell. With that the Hamiltonian with external electric field can be defined as:

$$\begin{aligned} H_E = &-\sum_i A_E \cos(6\varphi_i) - \sum_{\langle i,j\rangle} J_E \cos(\varphi_i - \varphi_j) \\ &- E \cdot p_0 \sum_i \cos(3\varphi_i)/N \end{aligned} \tag{4.4}$$

The ferroelectric transition with different lattice sizes is simulated under zero electric field with $J_E = J$, $A_E = \frac{5}{8}J$. The Z_6 order parameter m_{Z_6}, the polarization P, the heat capacity C and the density of Z_6 vortices ρ_v are plotted as functions of simulated temperature in Fig.4.2 (a), (b), (d) and (e), respectively. The simulation clearly showed two transitions: $T_{C1} \sim 1.8\ J/k_B$ marks the temperature where the vortex density drops, and $T_{C2} \sim 0.7\ J/k_B$ is associated with the onset of polarization. It is known that a 2D xy model does not yield any 1st or 2nd order phase transition, but can give rise to the Kosterliz-Thouless (KT) transition [113]. Previous theoretical works have shown that the 2D 6-state clock model can go from disorder to order through either an Ising transition plus a 3-state Potts transition or two KT transitions [114]. Numerical study on systems with similar Z_6 symmetry breaking shows evidences of 2 KT transitions with a critical phase in between [115, 116]. As shown in Fig.4.2 (a), (b), (d) and (e), the two transitions we observed exhibit little lattice-size dependence. Finite size scaling analysis on these two transitions supports

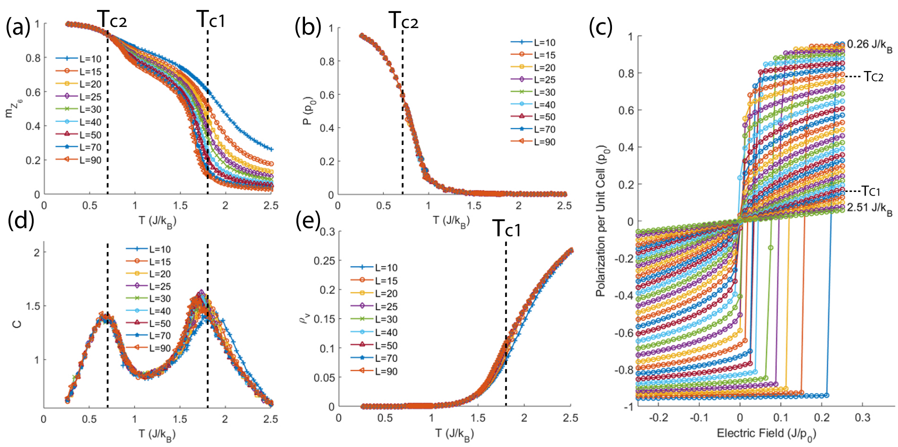

Figure 4.2 – Above shows the simulation results on the ferroelectric part of the model. First, the ferroelectric transition with different lattice sizes is simulated under zero electric field. The Z$_6$ *order parameter* m_{Z_6}*, the polarization* P*, the heat capacity* C *and the density of Z*$_6$ *vortices* ρ_v *are plotted as functions of simulated temperature in (a), (b), (d) and (e), respectively. Second, the responds of an* $L=40$ *lattice to the external electric field in temperature range of* $0.26 \sim 2.51\ J/k_B$ *are demonstrated in (c).*

neither Ising transition nor Potts transition. Therefore the two ferroelectric transitions in our model are most likely KT transitions. Shown in Fig.4.2 (c) are the simulation results of polarization as a function of the electric field E in a temperature range of $0.26 \sim 2.51\ J/k_B$ on a $L=40$ lattice. Initially the lattice was fully polarized by negative field. The external electric field was then gradually increased. The simulated lattice reached equilibrium at each field point. Below T_{C2} the system shows a clear ferroelectric hysteresis. Between T_{C2} and T_{C1} the system shows paraelectric behaviour with a non-linear P-E curve, similar to the superparaelectric P-E curve observed in relaxor ferroelectrics[117, 118]. Above T_{C1} the system becomes a normal paraelectric with linear P-E curve. The superparaelectric behavior between T_{C2} and T_{C1} suggest that the system is in a critical phase with infinite correlation length, which further supports that the two observed transition is KT type. The results of the simulation on the ferroelectric variable with zero electric field demonstrate that the Z_6 symmetry breaking in our model is achieved through two KT transitions. First the system breaks Z_3 symmetry, indicated by the decrease of vortex density, then the system breaks Z_2 symmetry, leading to non-zero polarization. This two-step nature of the ferroelectric transition in $RMnO_3$ has been observed experimentally [119]. The lattice responds to external electric field is in agreement with experimental results [109, 110, 120].

On top of the 6-fold clock model for ferroelectricity of the system, the 2D x-y model for magnetic order can be added by introducing the following Hamiltonian [121]:

$$H_S = -\sum_i A_S \cos(2\phi_i) - \sum_{\langle i,j\rangle} J_S \cos(\psi_i - \psi_j) \tag{4.5}$$

Here the variable ϕ_i represents the magnetic ordering within the ith unit cell, and the variable $\psi_i \equiv \varphi_i + \phi_i$ takes the ferroelectric domain of that unit cell into account. A_S represents the single-ion anisotropy for spin, and J_S is the coupling constant between the nearest neighbor $\langle i, j\rangle$. The magnetization per site in the j^{th} structural domain is calculated by:

$$M_j = \frac{\mu_0}{N_j}\left\{\left[\sum_i \cos(\phi_i)\right]^2 + \left[\sum_i \sin(\phi_i)\right]^2\right\}^{1/2} \tag{4.6}$$

with μ_0 representing the magnetic moment within a unit cell, and N_j being the size of the j^{th} domain. If fixing the ferroelectric variable $\varphi_i = 0$ across the whole lattice, the spin part of the model is equivalent to a 2D Ising model under strong anisotropy term A_S. By averaging amoung different structural domain the magnetic order parameter of the whole lattice is defined as:

$$M_S = \frac{1}{N}\sum_j N_j M_j \tag{4.7}$$

With only one structural domain, the magnetic order parameter is Ising like with reasonably large anisotropy A_S. It is then interesting to study how the magnetic transition behaves when the lattice exhibits different level of complexity in structural domain distribution. In the magnetic Hamiltonian H_S the nearest neighbor coupling term utilizes the combined order variable $\psi_i \equiv \varphi_i + \phi_i$, thus the magnetic long range order will be affected when going from one ferroelectric domain to another. Since the ferroelectric transition temperature of $RMnO_3$ is an order of magnitude larger than its magnetic transition temperature, the value of the parameters in H_S were chosen to be $A_S = J_S = 0.05J$. Shown in Fig.4.3 (a) are six 100×100 simulated lattices with different structural domain distributions. The 'slow cooled' lattice was simulated by gradually decreasing the temperature from above T_{C1} to $0.1J/k_B$. The 'quenched' lattices were simulated by abruptly

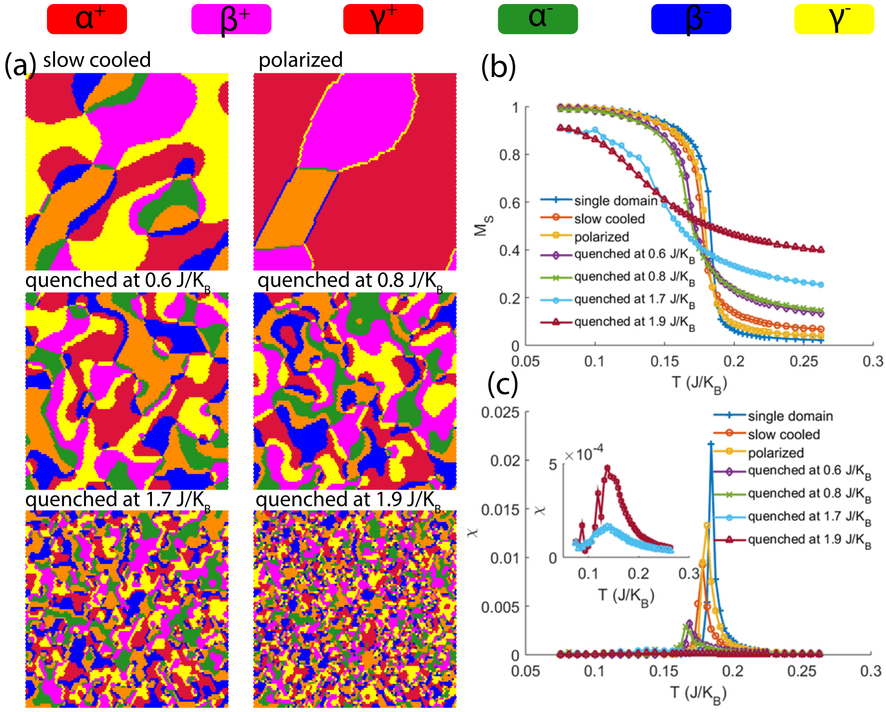

Figure 4.3 – Shown in (a) are six 100×100 simulated lattices with different structural domain distributions. The magnetic order parameters and susceptibilities of the six lattices plus a single domain case are plotted in (b) and (c) as functions of temperature. The inset in (c) are zoomed-in plot of the susceptibility curves of the last two quenched lattices.

changing the temperature from the labeled values to $0.1J/k_B$. The 'polarized' lattice was created by applying positive electric field on the 'slow cooled' lattice. The simulation results of the magnetic order on these lattices plus a trivial single domain case are shown in Fig.4.3 (b) and (c) in the form of magnetization and magnetic susceptibility. With increased structural domain complexity and decreased average domain size, the magnetic moments order with a lower transition temperature and a lower saturated magnetization at base temperature. Previous works have shown coupling between magnetoelastic coupling in this system using inelastic neutronscattering and ultrasonic measurements [122, 123]. In our model, the only thing that couples the magnetism and ferroelectricity is the $\sum_{\langle i,j \rangle} J_S \cos(\psi_i - \psi_j)$ term in Eq. (3), where the first nearest neighbor coupling of the magnetic moment is weakened if the two neighbors belong to different ferroelectric domains. When the structural domain becomes more complex, the frequently changing φ_i induces disorder in the coupling constant J_S, which drives the system towards the Edwards-Anderson model for spin glass [124]. In fact, the magnetic susceptibility curves of the 'quenched at 1.7 J/k_B' and 'quenched at 1.9 J/k_B' lattices shown in the inset of Fig.4.3 (c) is very similar to the no-field-cooling curve of a spin glass.

4.3 Summary

In the Monte Carlo simulation of the hexagonal rare earth mangtite system, a 6-fold clock model was used for the ferroelectric order and an x-y model with Heisenberg interaction and single ion anisotropy term was used for the magnetic order. The parameters representing the interaction strength for the ferroelectric order were chosen to be much larger than those for the magnetic order, simulating the well separated transition temperatures in the real system. In the simulation, the only overlap between the two ferroic orders was to use the sum of the two order variables in calculating the Heisenberg interaction of the spins. The simulation results demonstrated that the magnetism in the system can still be affected by an external electric field through the Z_6 structural domains under such a small coupling in the model, and that in extreme case the high vortex density can drive the system into a spin glass state.

Chapter 5

Neutron and X-ray study on the Fe Vacancy Ordering in Fe-based Superconductor $K_xFe_{2-y}Se_2$

5.1 Introduction

The coexistence and self-organization of multiple phases into complex morphologies provide for an electronic complexity that is at the heart of strongly correlated electron systems [56]. In the Fe-based and cuprate superconductors, superconductivity emerges by suppressing the static antiferromagnetic (AFM) order [52] but spin and charge density fluctuations persist, and are critical in the electron pairing mechanism. Coupled with these fluctuations is a heterogeneous lattice where the spatial interplay between the spin and charge degrees of freedom leads to nanoscale phase separation [19]. Thus the lattice structure is a signature of the phase separation and it is key to elucidating the symmetry-breaking ground state properties that allow superconductivity to evolve. The $A_xFe_{2-y}Se_2$ system is a test bed for exploring the very peculiar crystal symmetries that appear because of the close proximity of superconductivity to a magnetic insulating state, leading to a multiphase complex lattice whose precise nature has not been resolved, in spite of many studies. This has been in part due to inconsistent sample chemistry and an intricate vacancy ordering scheme that led to many different proposed crystal phases.

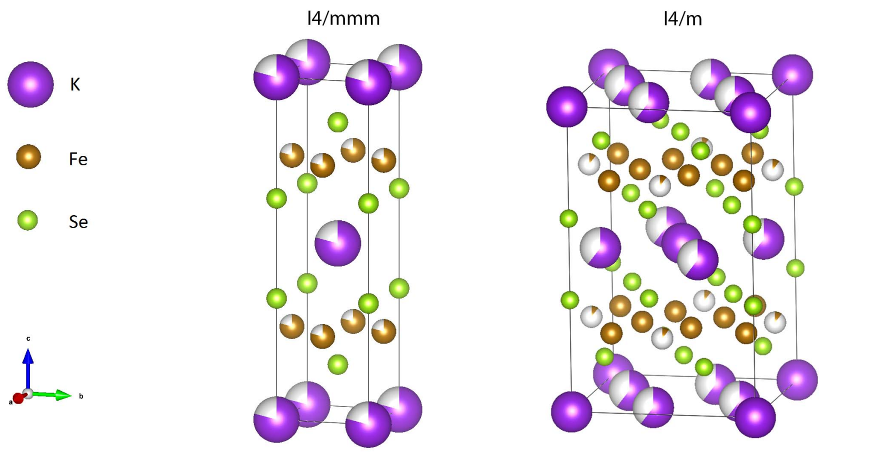

Figure 5.1 – Crystal structures of $K_xFe_{2-y}Se_2$ in its I4/mmm and I4/m phases.

The $A_xFe_{2-y}Se_2$ (A = K, Rb, Cs) iron selenide superconductor class has been intensely studied [125] in part due to the Fe-vacancy order and of its role in phase separation that may lead to SC and NSC regions [57, 58, 59, 60, 126]. With vacancies at both the A and

Fe sites, a well-known structural transition occurs when the Fe vacancies order at $T_S \sim 580\ K$[57]. Above T_S in the high temperature tetragonal phase with the *I4/mmm* space group, the vacancies are randomly distributed at both the Fe and A sites. Upon cooling below T_S, a superlattice structure appears due to Fe vacancy order. Several scenarios have been proposed regarding the nature of the microstructure below T_S. In one, the lattice is phase separated into a minority *I4/mmm* phase which is compressed in-plane and extended out-of-plane in comparison to the high temperature centrosymmetric phase and has no Fe vacancies, and a majority phase with the Fe vacancies ordered in different superlattice patterns [127, 128, 129, 130]. The most commonly reported superlattice structure with Fe vacancy order is the $\sqrt{5} \times \sqrt{5} \times 1$ with space group *I4/m* [57, 126, 131, 132]. The crystal structures of the $K_xFe_{2-y}Se_2$ in its *I4/mmm* and *I4/m* phases are plotted in Fig. 5.1. More recently, other superlattice patterns have been reported in the literature such as the $2 \times 2 \times 1$ [126, 133], the $1 \times 2 \times 1$ [58, 126, 133, 134] and the $\sqrt{8} \times \sqrt{10} \times 1$ [59].

The distinction among the different superlattice patterns arises from the underlying order of the Fe and alkali metal sublattices. As illustrated in Fig. 5.1, in the superstructure with space group *I4/m*, the Fe site symmetry is broken from the high temperature *I4/mmm* space group, giving rise to two crystallographic sites. Preferred site occupancy leads to the $\sqrt{5} \times \sqrt{5}$ supercell, in which one site is empty (or sparsely occupied) while the other is almost full. Magnetic ordering is characteristic of this phase. Below $T_N \sim 560\ K$, AFM ordering arises in the *I4/m* phase and persists well below T_c[57]. The AFM magnetic state [57, 58, 131] is robust unlike what has been reported in other Fe-based superconductors, and its coexistence with the superconducting state has raised concerns about the validity of the s+/- coupling mechanism coupled with the absence of hole pockets at the Fermi surface and the lack of nesting in this system[135]. More recently, evidence of alkali site vacancy order has been presented as well with a $\sqrt{2} \times \sqrt{2}$ superlattice structure within the *I4/mmm* phase in $K_xFe_{2-y}Se_2$[127] and $Cs_xFe_{2-y}Se_2$[136, 137, 138]. The centrosymmetry of the *I4/mmm* is broken due to the alkali metal order. The *I4/mmm* phase with no Fe vacancy has largely been attributed to be the host of superconductivity in part because of the absence of magnetism and vacancies.

It is understood at present that by post-annealing and quenching, superconductivity can be controlled in this system [139, 140] even though the actual mechanism remains unknown. Magnetic refinement from neutron powder diffraction measurements revealed that magnetic order does not exclude the presence of a SC phase[141]. Moreover, a smaller magnetic moment was refined in NSC crystals indicating no correlation of the absence of magnetism and superconductivity. To identify which crystal phases are present, high-energy X-ray scattering measurements were performed on two kinds of $K_xFe_{2-y}Se_2$ single crystals, one annealed and SC, and the other as-grown and NSC. In combination with Monte Carlo simulations, it is shown that superconductivity in the annealed and quenched crystal is most likely present in regions where the $\sqrt{5} \times \sqrt{5} \times 1$ Fe vacancy ordered *I4/m* phase borders the *I4/mmm* domains with no Fe vacancies. The in-between region consists of an non-magnetic Fe vacancy disorder phase. Thus superconductivity in this system appears at the crossover of the vacancy order-disorder transition. Quenching increases the boundary walls around the *I4/m* domains, leading to an increase of the percolation paths and an enhancement of superconductivity.

5.2 Experimental results

Single crystals of $K_xFe_{2-y}Se_2$ were grown using the self-flux method. The first step of the synthesis involved the preparation of high-purity FeSe by solid state reaction. Stoichiometric quantities of iron pieces (Alfa Aesar; 99.99%) and selenium powder (Alfa Aesar; 99.999%) were sealed in an evacuated quartz tube, and heated to 1075 °C for 30 hours, then annealed at 400 °C for 50 hours, and finally quenched in liquid nitrogen. In the second step, a potassium grain and FeSe powder with a nominal composition of K:FeSe = 0.8:2 were placed in an alumina crucible and double-sealed in a quartz tube backfilled with ultrahigh-purity argon gas. All samples were heated at 1030 °C for 2 hours, cooled down to 750 °C at a rate of 6 °/hr, and then cooled to room temperature by switching off the furnace. High quality single crystals were mechanically cleaved from the solid chunks. In the final step, the annealed crystals were additionally thermally treated at 350 °C under argon gas for 2 hours, followed by quenching in liquid nitrogen. The crystals that were not heat-treated were labeled as-grown. The magnetic susceptibility and transport were measured from 2 to 300 K and the as-grown crystal is NSC while the annealed crystal is SC. Back-scattered scanning electron microscopy (SEM) measurements were carried out at room temperature on the two samples[141]. The characterization of these crystals was previously reported in Ref.[141]. The SEM measurements showed that the surface morphology of the as-grown crystal has two kinds of regions: rectangular islands with a bright color and a background with a dark color. On the other hand, instead of island-like domains, very small bright dots were observed on the surface of the annealed crystal. Specific heat measurements performed on the SC crystals showed no transition at $T_c \sim 29\ K$, as seen in Figs. 5.2 (e) and (f), indicating that it does not exhibit bulk superconductivity. The single crystal diffraction measurements were carried out at the Advanced Photon Source of Argonne National Laboratory, at the 11-ID-C beam line. In-plane and out-of-plane measurements were carried out on both types of crystals at room temperature.

The X-ray diffraction from the *hk0* scattering plane shows evidence of coexistence of multiple phases, consistent with earlier measurements. Shown in Figs. 5.2(a) and 1(b) are the patterns corresponding to the as-grown and quenched crystals, respectively. Several features are observed in both samples that arise from the presence of the two configura-

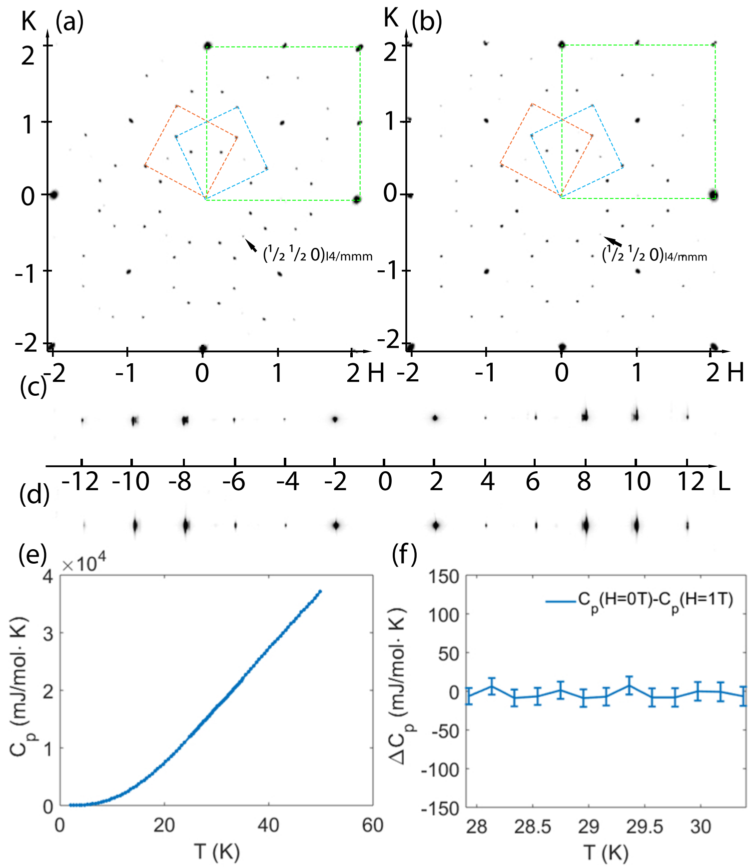

Figure 5.2 – The diffraction patterns from the hk0 plane from (a) as-grown and (b) quenched crystals. In (c) and (d) are the plots along the 00l direction in the as-grown and quenched crystal, respectively. The hk0 patterns consist of two configurations of the I4/m phase highlighted by the two inner dashed boxes, and the I4/mmm phase with a $\sqrt{2}\times\sqrt{2}$ superlattice structure highlighted by the outer dashed box. Subplot (e) shows the specific heat measurement of the SC sample at zero magnetic field (0 T). (f) is the difference of the SC sample's specific heat data at 0 T and 1 T in the vicinity of $T_c \sim 29\ K$.

tions of $\sqrt{5}\times\sqrt{5}\times 1$ superlattice structure with the *I4/m* symmetry [127, 132] indicated by the two inner dashed boxes as well as the *I4/mmm* phase indicated by the outer dashed box. The arrow points to a superlattice peak indexed to ($\frac{1}{2}$ $\frac{1}{2}$ 0). The lattice constant calculated from this peak position matches that of the *I4/mmm* phase with a $\sqrt{2}\times\sqrt{2}$ A-site vacancy order. The scattering patterns along the *l*-direction are shown in Figs. 5.2(c) and (d) for the as-grown and quenched crystals, respectively. Bragg peaks from *I4/mmm* appear at the lower Q side of the *I4/m* peaks. Neither l=2n+1 superlattice peaks nor diffuse scattering are observed along the (00l) direction, leaving the out-of-plane stacking of the $\sqrt{2}\times\sqrt{2}$ K-vacancy order unclear. Due to sample rotation during measurement, weak

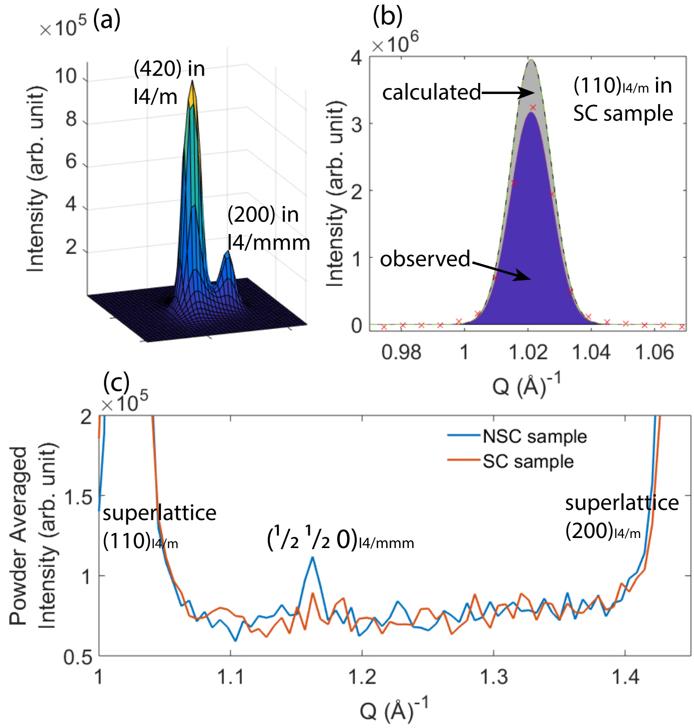

Figure 5.3 – (a) A comparison between Bragg peaks from I4/m and I4/mmm phases. (b) The observed superlattice peak (110) in SC crystal is compared with the calculated intensity based on an ideal I4/m structure. (c) The powder integral of the hk0 scattering plane in the vicinity of the superlattice peak ($\frac{1}{2}$ $\frac{1}{2}$ 0).

reflections are observed at the lower Q and higher Q sides of the (006) and (00$\bar{6}$) Bragg peaks, and can be indexed to the (204) and (206) Bragg peaks, respectively.

In both crystals, the diffraction pattern is dominated by a majority phase with the *I4/m* space group with Fe vacancies and a minority phase consisting of the high symmetry *I4/mmm* space group with no vacancies at the Fe site and a weak $\sqrt{2}\times\sqrt{2}$ vacancy order at the K site. Shown in Fig. 5.3(a) are the (200) Bragg peak from the *I4/mmm* minority phase and the (420) Bragg peak from the *I4/m* majority phase in the *hk0* plane. They are well-resolved given that the two phases have different lattice constants ($a/\sqrt{5}\sim$3.90 Å in *I4/m*, $a\sim$3.84 Å in *I4/mmm*), often difficult to see in powders. Shown in Fig. 5.3(c) are the powder integrated diffraction patterns obtained from the annealed and as-grown crystals in the vicinity of the ($\frac{1}{2}$ $\frac{1}{2}$ 0) superlattice peak. Even though this peak is observed in both diffraction patterns, it is significantly stronger and clearly above the background level in the as-grown crystal at $Q \sim 1.16$ Å^{-1} but barely visible in the annealed sample. The ($\frac{1}{2}$ $\frac{1}{2}$

Table 5.1 – Refined structure parameters for the I4/m phase that includes both the Fe-vacancy disordered and Fe-vacancy ordered phases. Atomic position: K1, 2a $(0,0,0)$; K2, 8h $(x,y,0)$; Fe1, 4d $(0,\frac{1}{2},\frac{1}{4})$; Fe2, 16i $(x,y,0.2515)$; Se1, 4e $(\frac{1}{2},\frac{1}{2},0.1351)$; Se2, 16i $(x,y,0.1462)$. Out-of-plane coordinates are not refined, values are from ref[57]. If not listed, the site occupancy (Occ.) is 1.

		SC	NSC
	a(Å)	8.7261(7)	8.7243(5)
	c(Å)	14.108(4)	14.104(4)
K1	Occ.	0.75(7)	0.73(7)
	U_{iso}	0.046(7)	0.050(6)
K2	x	0.376(4)	0.377(2)
	y	0.196(2)	0.211(2)
	Occ.	0.73(7)	0.76(6)
	U_{iso}	0.046(7)	0.050(6)
Fe1	Occ.	-0.04(2)	-0.06(2)
	U_{iso}	0.016(3)	0.023(2)
Fe2	x	0.1990(4)	0.1979(3)
	y	0.0898(5)	0.0876(5)
	Occ.	0.90(2)	1.02(1)
	U_{iso}	0.016(3)	0.023(2)
Se1	U_{iso}	0.010(2)	0.018(1)
Se2	x	0.1070(4)	0.1083(3)
	y	0.3012(3)	0.3028(2)
	U_{iso}	0.010(2)	0.018(1)
wR		6.7%	5.0%
volume frac.		73(1)%	66.5(6)%

0) peak is not as intense as the other superlattice features which suggests that the K-site vacancy is partially ordered in the *I4/mmm* phase. The K-site vacancy order can break the symmetry of the centrosymmetric *I4/mmm* to *P4/mmm* or to an even lower symmetry depending on its out-of-plane stacking pattern. However, our out-of-plane diffraction data did not provide enough information to further confirm the new symmetry. Single crystal refinement was performed on the *hk0* plane data, and the results are summarized in Tables 5.1 and 5.2, where space group *P4/mmm* was used to refine the ($\frac{1}{2}$ $\frac{1}{2}$ 0) superlattice peak of the minority phase. How the K vacancy order affects superconductivity is still an open question. The refinement yielded a volume fraction for the *I4/mmm* phase of 27(1)% in the annealed sample and about 33.5(6)% in the as-grown. At the same time, the refinement indicates that the *I4/m* phase is not fully ordered with the $\sqrt{5}\times\sqrt{5}\times 1$ Fe vacancy ordered supercell (detailed discussion can be found in Appendix). Shown in Fig. 5.3(b) is a comparison of the integrated intensity of the (110)$_{I4/m}$ superlattice peak to the calculated intensity assuming a fully ordered Fe-vacancy. The experimental inten-

Table 5.2 – Refined structure parameters for the P4/mmm Fe-vacancy free phase. Atomic position: K1, 1a $(0,0,0)$; K2, 2e $(\frac{1}{2},0,\frac{1}{2})$; K3, 1c $(\frac{1}{2},\frac{1}{2},0)$; Fe1, 8r $(x,x,0.25)$; Se1, 2g $(0,0,0.1456)$; Se2, 2h $(\frac{1}{2},\frac{1}{2},0.1456)$; Se3, 4i $(0,\frac{1}{2},0.3544)$. Out-of-plane coordinates are not refined, values are from ref[57]. If not listed, the site occupancy (Occ.) is 1.

		SC	NSC
	a(Å)	5.437(1)	5.433(1)
	c(Å)	14.230(7)	14.237(2)
K1, K2	U_{iso}	0.03(1)	0.068(4)
K3	Occ.	0.47(5)	0.52(1)
	U_{iso}	0.03(1)	0.068(4)
Fe1	x	0.249(1)	0.244(1)
	U_{iso}	0.039(5)	0.023(1)
Se1, Se2, Se3	U_{iso}	0.023(3)	0.029(1)
wR		6.1%	1.4%
volume frac.		27(1)%	33.5(6)%

sity is reduced which shows that even within the I4/m majority phase, the Fe vacancies are not fully ordered. Two different Fe vacancy schemes are present within the I4/m superstructure, one with fully ordered Fe vacancies and AFM order and one with partially ordered (or disordered) vacancies and non-magnetic. Focusing on the disordered Fe sublattice it is indistinguishable from the ordered Fe sublattice because their lattice constants are unresolved in the experimental data. The I4/m phase evolves continuously from the high temperature I4/mmm as shown by Ricci et al in Ref.[127]. The I4/mmm was used to represent the Fe disordered sublattice. High pressure experiments are planned next to distinguish the Fe ordered from the Fe disordered sub lattice.

5.3 Summary

The Fe-based superconductor $K_xFe_{2-y}Se_2$ is known to phase separate into a Fe-vacancy ordered antiferromagnetic phase and a Fe-vacancy free non-magnetic phase. As-grown sample showed island-like domains of vacancy ordered phase under scanning electron microscopy. Anneal and quench the sample after it was prepared can improve the sample homogeneity as well as increase the superconducting shielding fraction from below 5% to around 75 %. Below superconducting temperature, the quenched sample still showed large magnetic moment, suggesting that the vacancy ordered phase is not the superconducting phase. By single crystal refinement, volume fraction of the vacancy free phase were obtained for both quenched and as-grown sample. The superconducting quenched sample had less vacancy free phase volume fraction comparing to the non-superconducting as-grown sample, indicating that the vacancy free phase is not superconducting either. The occupation number of the Fe2 site from the refinement implied that the thermal treatment of post-annealing and quenching induced vacancy disorder in the sample, which could be related to superconductivity.

Chapter 6

Monte Carlo Simulation on the Fe Vacancy Ordering in Fe-based Superconductor $K_xFe_{2-y}Se_2$

6.1 Introduction

It is known that the superconducting shielding fraction of $K_xFe_{2-y}Se_2$ can be enhanced by annealing the sample above T_S followed by quenching [139, 140]. Scanning electron microscopy (SEM) studies showed that the post annealing and quenching process can affect the spatial domain distribution [141]. Before thermal treatment, the as grown sample shows islands of vacancy free $I4/mmm$ domains surrounded by $I4/m$ domains on the cleaved surface. After quenching, the surface loses the island pattern and becomes more homogeneous. A scanning photoelectron microscopy (SPEM) study demonstrated the existence of a filamentary network of the superconducting phase in the quenched sample [142]. The superconducting phase has been assumed to be the Fe vacancy free $I4/mmm$ phase partly due to the connection between the enhancement of the superconducting shielding fraction under thermal treatment and the Fe vacancy free $I4/mmm$ phase change from islands to a more homogeneous distribution under the same thermal process. However, by simulating the post annealing and quenching process on a quasi-2D Fe-sublattice using the Metropolis Monte Carlo algorithm with an Ising-like Hamiltonian, we found that a third phase stands out as a result of freezing the high temperature vacancy disordered $I4/mmm$ phase during quenching, serving as a candidate for the superconducting phase.

6.2 Monte Carlo Simulation

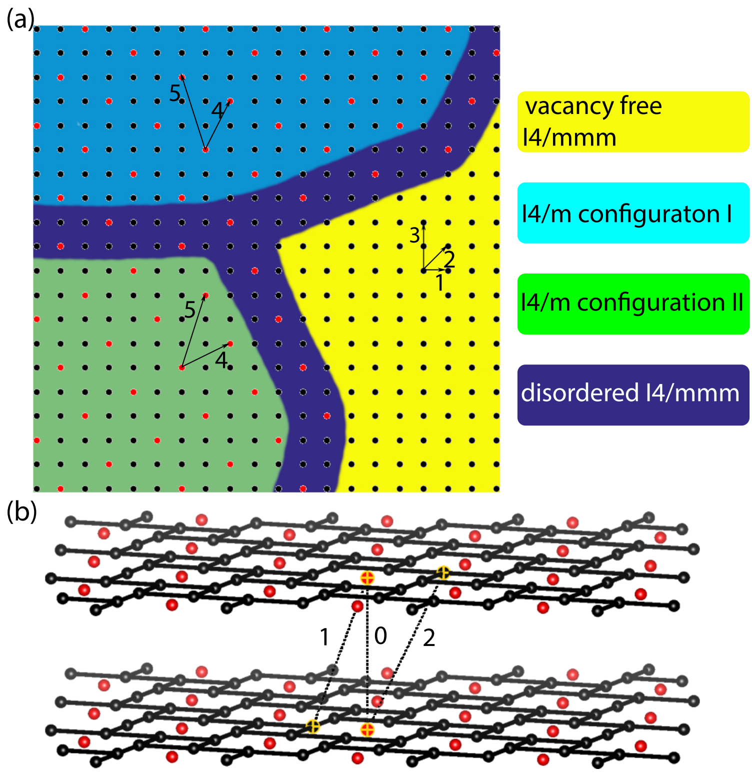

Figure 6.1 – Shown in (a) is a schematic ab-plane of the simulated lattice, demonstrating four types of domain: the vacancy free $I4/mmm$ phase (yellow), two configuration of the $\sqrt{5}\times\sqrt{5}\times 1$ vacancy order phase (light blue, green), and the disordered $I4/mmm$ phase (dark blue). The black (red) dots represent Fe atom (vacancy). The n^{th} intra-plane nearest neighbor coupling constants J_n^{ab} is illustrated here up to $n = 5$. Subplot (b) shows the n^{th} inter-plane nearest neighbor coupling constants J_n^c from $n = 0$ to 2.

The Monte Carlo simulation used in this work is defined on the Fe sublattice only, and is based on the Metropolis algorithm. The Hamiltonian is constructed using an Ising-like general form of $H = \sum_{n=1}^{N_{ab}} \sum_{\langle i,j\rangle_n^{ab}} J_n^{ab} \sigma_i \sigma_j + \sum_{n=0}^{N_c} \sum_{\langle i,j\rangle_n^c} J_n^c \sigma_i \sigma_j$. The Ising variable $\sigma_i = \pm 1$ represents the occupancy of the site i, with +1 for an Fe ion and -1 for a vacancy. The coupling constants $J_n^{ab,c}$ are defined over the n^{th} nearest neighbor pair $\langle i,j\rangle_n^{ab,c}$ in the ab-plane or between adjacent layers along c, respectively, as shown in Fig. 6.1. Since both the high symmetry $I4/mmm$ phase and the vacancy ordered $\sqrt{5}\times\sqrt{5}\times 1$ phase have a quasi-2D nature, the Hamiltonian will have strong intra-plane coupling and weak inter-plane coupling, which is achieved by the difference in the magnitude and total number of coupling constants defined for the intra- and inter-plane. The Monte Carlo step is chosen to site swap to conserve the total vacancy number, since the vacancy to Fe ion ratio in the sample is not changing during the thermal treatment. For each Monte Carlo step, a pair of i and j sites is randomly chosen, and is swapped with a probability of $MIN(1, e^{-\Delta E/T})$, where ΔE represents the energy change caused by the swap, and $MIN()$ returns the minimum value of the input. The simulation runs on a simple tetragonal lattice with periodic boundary condition, where each ab-plane is a square lattice, simulating the Fe-sublattice in ab-plane of $A_xFe_{2-y}Se_2$. Since this is a simple simulation model focusing on the Fe vacancy pattern, other factors such as thermal vibrations, site distortions and differences in lattice constants between the phases are not considered.

To get the $\sqrt{5} \times \sqrt{5}$ vacancy order, the intra-plane coupling J_n^{ab} must be defined at least up to $N_{ab} = 5$ with J_1^{ab}, J_2^{ab}, $J_3^{ab} > 0$ and J_4^{ab}, $J_5^{ab} < 0$. A perfect $\sqrt{5} \times \sqrt{5} \times 1$ pattern has 20% of vacancies, thus if the vacancy ratio is lower than 20%, part of the simulated lattice will have no vacancy, representing the vacancy free $I4/mmm$ phase. The ground state of such lattice will consist of one $I4/m$ domain and one vacancy free $I4/mmm$ domain with a domain distribution that minimizes the length of the domain wall. At a finite temperature below T_S, the two configurations of the $I4/m$ phase should appear with equal probability, since the coupling constants J_4^{ab} and J_5^{ab} do not distinguish between them. When $T > T_S$, the vacancies should be randomly distributed. If a vacancy is found in an incomplete $\sqrt{5} \times \sqrt{5} \times 1$ environment, this site as well as its nearest neighbors will be assigned to a disordered $I4/mmm$ phase. Four types of domains can be defined on the simulated lattice, as illustrated in a schematic plot Fig. 6.1(a).

The inter-plane coupling constants can affect the transition temperature, but do not contribute to the vacancy order or domain distribution. In this work the simulation is carried out on a $200 \times 200 \times 5$ lattice with 15% vacancies, and the coupling constants in the Hamiltonian are defined up to the 5^{th} intra-plane nearest neighbor and the 1^{st} inter-plane nearest neighbor with the following values: $J_0^c = -3.0$, $J_1^{ab} = 10.0$, $J_2^{ab} = 8.0$, $J_3^{ab} = 8.0$ï¼Œ $J_4^{ab} = -6.5$, $J_5^{ab} = -6.5$.

Fig. 6.2(a) is a plot of the total energy as a function of the simulation temperature, in which a typical Ising-like phase transition is observed at T~ 35. Fig. 6.2(b) shows the change of volume fractions of each phase in the same temperature range. It is clear that

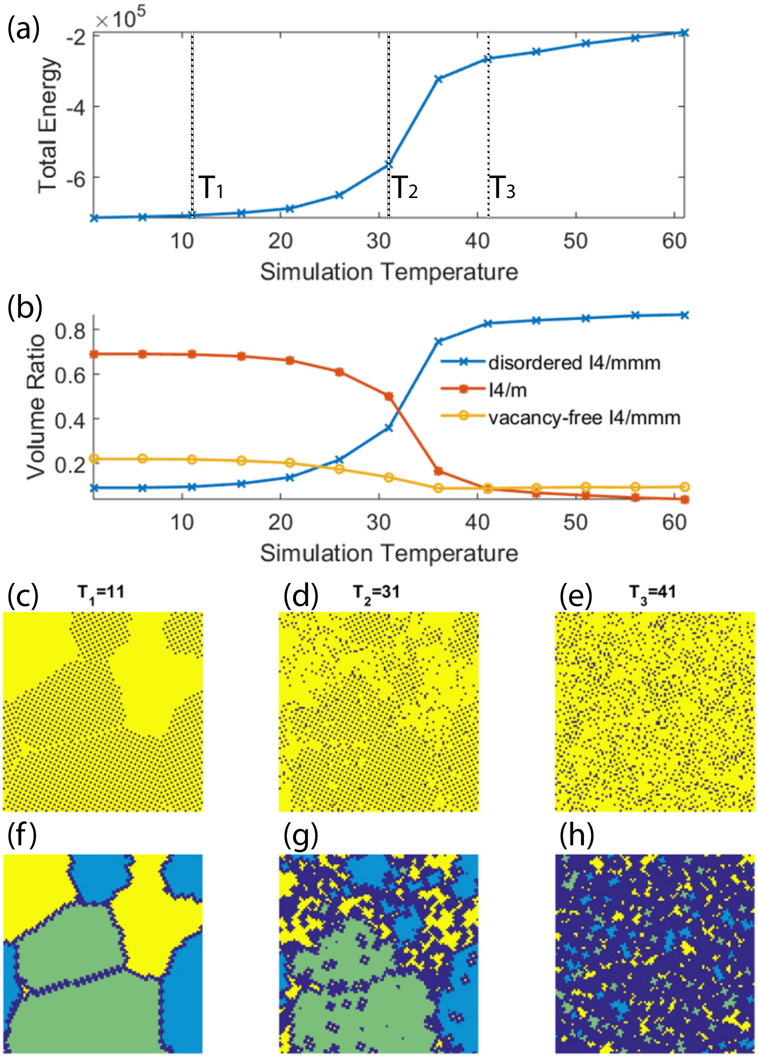

Figure 6.2 – In (a) the total energy of the simulated lattice is plotted as a function of temperature. In (b) the volume ratio of each phase is plotted as a function of temperature. (c)-(e) show Fe vacancies (black dots) on a $100 \times 100 \times 1$ region of the simulated lattice at temperature $T_1 = 11$, $T_2 = 31$, $T_3 = 41$, respectively, as indicated by the dashed lines in (a). (f)-(h) show the same region but with each phase painted using the color shown in figure 1 (a).

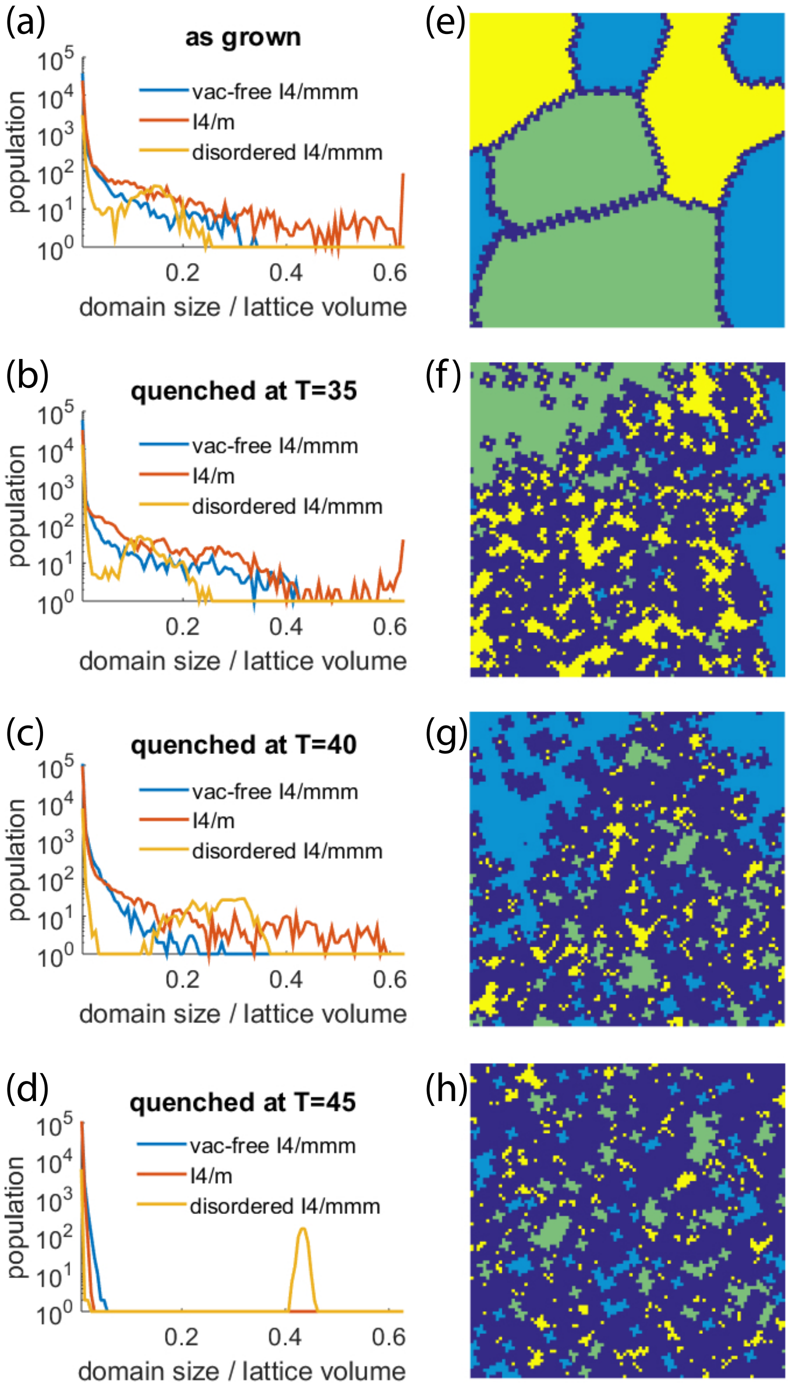

Figure 6.3 – Shown above are population of domain size as well as domain distribution in ab-plane from four simulated lattices: (a) and (e) are as grown sample, (b) and (f) are quenched at T=35, (c) and (g) at T=40, (d) and (h) at T=45. Note: the x axis in (a)-(d) is the ratio of the volume size over the total lattice volume.

the Ising-like transition simulated by the Hamiltonian is a transition from a vacancy disordered phase to a $\sqrt{5} \times \sqrt{5} \times 1$ vacancy ordered phase. This indicates that the constructed Hamiltonian and the choice of coupling constants are suitable to modeling the structural phase transition from the high temperature $I4/mmm$ phase to the vacancy ordered $I4/m$ phase in the $A_xFe_{2-y}Se_2$ system.

The vacancy and domain distributions of the simulated lattice at three typical simulated temperature points $T_1 = 11$, $T_2 = 31$, $T_3 = 41$ are shown in Figs. 6.2(c)-(h). At low temperature, both the vacancy free $I4/mmm$ phase and the two configurations of the $I4/m$ phase grow into big domains, while the disordered $I4/mmm$ is mainly located on the domain walls. When the lattice warms up towards the transition, vacancies start to lose the $\sqrt{5} \times \sqrt{5} \times 1$ pattern, and the disordered $I4/mmm$ phase emerges in the big domains. Above the transition temperature, the simulated lattice is dominated by the disordered $I4/mmm$ phase, and the other phases form small islands that scatter over the lattice.

To simulate the effects of annealing and quenching, a simulated lattice which has equilibrated at low temperatures (as grown) is brought to high temperatures (higher than T_S). Once the lattice reaches the high temperature equilibrium, the temperature is set back to base temperature directly. After the thermal treatment, the size of each domain is calculated, and the population of each type of domain over 100 simulated lattices is analyzed. Fig. 6.3 shows the domain size population ((a)-(d)) and domain distribution ((e)-(h)) for the as grown lattice and for a lattice quenched at T=35, 40, 45. The domain distribution of the quenched lattices show a significant increase of disordered $I4/mmm$ phase. The domain size population plots clearly show that the population of the disordered $I4/mmm$ domains become larger as the quenching is carried out at higher simulated temperatures. When the lattice is quenched at T=45, the disordered $I4/mmm$ domain with a size over 40% of the whole lattice dominates. This indicates that the high temperature phase freezes during the quenching process at a high annealing temperature (i.e. T=45), leaving the disordered $I4/mmm$ phase spreading over the lattice.

6.3 Summary

The SC crystal has less of the *I4/mmm* phase with no Fe vacancies than the NSC crystal. Furthermore, the simulation results indicate that the SC crystal tends to form more domain boundaries with the Fe-vacancy disordered phase sandwiched between the *I4/mmm* vacancy free and the *I4/m* vacancy ordered phases as seen in Fig 6.3(d), and very possibly leads to superconductivity in a filamentary form, in agreement with a reported SPEM study [142]. Theory work based on DFT calculation from T. Berlijn *et al.* also suggested that randomly distributed Fe vacancies can lead to effective doping, and can preserve the band structure from being destroyed as in the Fe vacancy ordered *I4/m* phase [143]. The enhancement of superconductivity as well as the filamentary nature of the superconductivity in this compound is attributed to the increase of domain walls by annealing and quenching.

Chapter 7

Discussion

7.1 Discussion on the multiferroic $RMnO_3$

Multiferroic materials have drawn the attention of the condensed matter community in the past few decades for the potentials of finding electric field controlled spintronics or magnetic field controlled electronics. Unfortunately, having ferroelectricity and (anti)ferromagnetism in a single phase of a material does not spontaneously lead to strong coupling between the two orders. One possibility of strong magnetoelectric coupling is in type-II multiferroics where magnetism is the cause of ferroelectricity. The downsides are the low transition temperature and the relatively small magnetic moment and electric polarization. Recently, magnetic order induced dielectric constant anomaly was observed in type-I multiferroics with frustrated magnetic structures such as the hexagonal rare earth manganites. These materials have ferroelectric transition at $500\ K \sim 1000\ K$ and (anti)ferromagnetic transition around $50\ K \sim 100\ K$ with reasonable magnetic moment and electric polarization. Although very weak, the observed coupling between the ferroic orders is a promising sign of potential magnetic field controlled electronics. Meanwhile, it is also interesting to investigate the possible electric field effects on the magnetic order in multiferroics with frustrated magnetism.

Neutron scattering and Monte Carlo simulation results on the electric field induced magnetic ordering enhancement in the hexagonal rare earth manganites $RMnO_3$ (R = Y, Lu, Sc,$\cdots$) were discussed in chapter 3 and 4 [90]. As a typical type-I multiferroic material, the hexagonal $RMnO_3$ has different mechanisms for the ferroelectricity and antiferromagnetism. The ferroelectric transition at $T_C \sim 900\ K$ is due to the tilting of the MnO_5 bipyramid towards one of the three rare earth atoms in the unit cell. This process, also known as trimerization [77], breaks the lattice symmetry from *P*6_3*/mmc* to *P*6_3*cm* and creates 6 ferroelectric domains. At around 90 K, the spins of the Mn atoms order in a 120° arrangement. Apart from the reported dielectric anomaly at magnetic transition temperature [106], our single crystal neutron scattering experiments on $LuMnO_3$ demonstrated an increase of the magnetic Bragg peak intensity near the magnetic transition temperature. The enhancement was observed only when applying electric field along one direction of a fresh sample, and reversing the field did not show an opposite effect. From second harmonic generation results it was shown that the ferroelectric domain walls also serve as antiferromagnetic domain walls [20]. It was therefore a natural inference to attribute the observed magnetic ordering enhancement as a result of domain wall motion under electric field. A Monte Carlo simulation was performed to confirm the proposed explanation. For the ferroelectric order, a 6-state clock model was used to capture the nature of the 6 ferroelectric domains. For the magnetic order, a 2D x-y model with a 2-fold anisotropy was used. By adding the ferroelectric order variable to the magnetic one in calculating nearest neighbor interactions, the coupling through domain walls was simulated. The results of the simulation indicate that the magnetic transition temperature is a function of the ferroelectric domain distribution. The simulated samples with more ferroelectric domains have lower transition temperatures, and in the extreme case the system starts to show spin glass/liquid behaviour.

In hexagonal $RMnO_3$, the magnetic and electric orders are not competing with each other. It is the long range magnetic order and the structural defects at the ferroelectric domain walls that are competing. The Heisenberg and the Dzyaloshinskii–Moriya interactions of the system will be interrupted while going from one ferroelectric domain to the adjacent one, causing the high density of ferroelectric domain walls to delay the magnetic transition to lower temperature. External electric field therefore has a secondary effect on the magnetic ordering through changing the domain topology.

7.2 Discussion on the Fe-based Superconductor $K_xFe_{2-y}Se_2$

The pursuing for room temperature superconductivity has always been a major focus among the condensed matter society. So far the highest critical temperature reported under ambient pressure is $133\ K$ in the Hg-Ba-Ca-Cu-O cuprate superconductor [144]. In cuprates, superconductivity competes with the long range antiferromagnetic order, and the spin fluctuation when the antiferromagnetic order disappears is believed to be related to Cooper pairing. The microscopic pairing mechanism for cuprates still remains controversial, and the anticorrelation between the charge-density-wave peddles and the quench disorder seems to play a role [19]. The first Fe-based superconductor was discovered in 2008, and has developed into a whole family of Fe pnictides and chalcogenides with $T_c \sim 10\ K$ to $50\ K$ [43, 51]. Having superconductivity in a system consisting of iron, a strong magnetic element, is already counterintuitive. And with new features such as nearly cylindrical electron and hold pockets, nematicities in electron structures, and vacancy orderings, Fe-based superconductors have quickly become the key topic in the community.

The Fe vacancy ordering in the Fe-based Superconductor $K_xFe_{2-y}Se_2$ was discussed both experimentally [55, 91] and computationally [91, 92] in chapter 5 and 6, respectively. $K_xFe_{2-y}Se_2$ has a complex phase diagram due to the vacancy on both the K site and the Fe site. The absence of hole pockets at Fermi level shown by ARPES measurements distinguishes it from the iron pnictide family, and ruled out the possibility of having Fermi surface nesting model and $s^{\pm}$-wave gap symmetry [54]. Superconductivity in this system is reported to be associated with a region on the phase diagram where the system phase separates into a $\sqrt{5} \times \sqrt{5}$ Fe-vacancy ordered phase and a Fe-vacancy free phase [127]. A checkerboard antiferromagnetic order was observed in the Fe-vacancy ordered phase in the superconducting state, indicating that the superconductivity does not arise from this phase [51]. By comparing the neutron and x-ray diffraction patterns of a superconducting and a non-superconducting samples, the volume ratios of the Fe-vacancy free and Fe-vacancy ordered phases were extracted. The quenched and superconducting sample did not show large volume fraction of the Fe-vacancy free phase. On the contrary, it showed less of the Fe-vacancy free phase compared to the as-grown and non-superconducting sample. The refinement on the crystal structures of the two phases in each sample implied a significant amount of randomly distributed Fe-vacancy in the quenched sample. A Monte Carlo model on the Fe sublattice was constructed to simulate the Fe vacancy distribution under different thermal treatment: quenched and as-grown. The Fe-vacancy disorder state increased significantly at the domain boundaries under simulated quenching, resulting in a filamentary network of disordered Fe-vacancy. With supporting results from other groups [19, 143], the superconductivity in $K_xFe_{2-y}Se_2$ system is attributed to this Fe-vacancy disorder phase at the domain boundaries.

In this system, the competing orders are superconductivity and the Fe-vacancy order. In the Fe-vacancy free phase, band structure calculations at the Fermi level show clear electron pockets at the zone corners and hole pockets at the zone center. When the Fe vacancies fully order in the $\sqrt{5} \times \sqrt{5}$ pattern, a strong Fermi surface reconstruction is expected due to the strong scattering against the Fe vacancies, resulting in antiferromagnetism and suppression of superconductivity. With randomly distributed vacancies, *ab initio* calculation with configuration average shows a dispersive band structure very similar to the one from the Fe-vacancy free phase, but with an effective doping which raises the Fermi level above the hole pockets and can even create electron pockets at the zone center [143]. The calculated Fermi surface of the Fe-vacancy disordered phase agrees very well with ARPES results in this systems [54, 135], indicating that the disordered Fe vacancies are the main contributor to the Fermi surfaces observed experimentally. With post-annealing and quenching, the inhomogeneity of the domain topology is reduced, the Fe-vacancy ordering is suppressed, and the resulting increase of the randomly distributed vacancies can cause effective doping and lead to superconductivity.

Chapter 8

Conclusion

Neutron and x-ray scattering are very import techniques in determining the static and dynamic details of crystal structures. When performed on single crystal sample, the extra information such as peak profile, diffuse scattering, and volume ratio of twin structures can be used to reconstruct the bulk domain topology to some extent, which is beyond the reach of surface probes such as scanning/tunneling electron microscopy and second harmonic generation. Together with Monte Carlo simulations, the domain topology of the sample can be studied.

The domain topology in a strongly correlated material with competing orders can be related to novel properties such as coupling between multiferroic orders and superconductivity. In hexagonal multiferroic $RMnO_3$, both magnetic and electric orders are related to the lattice distrotion called trimerization, leading to an electric field effect on the magnetic ordering through domain walls between different trimerization center. In Fe-based superconductor $K_xFe_{2-y}Se_2$, superconductivity occurs at the proximity of a $\sqrt{5}\times\sqrt{5}$ Fe-vacancy ordered phase and an Fe-vacancy free phase. Changing the domain topology through post-annealing and quenching induces randomness to the Fe-vacancy order, leading to superconductivity. In many systems with strong electron-electron correlations, samples with complex spatial domain distributions are common. A interplay between the competing order parameters can be embedded in the domain topology. It is therefore necessary to study what kind of effects the domain topology may have. When different order parameters are competing with each other, domains that are associated with one of the orders may be tuned through temperature or external field, allowing an effective control on the other order.

Apart from multiferroics and Fe-based high-T_c superconductors, there are many other strongly correlated systems with competing orders. Examples include long-range antiferromagnetic order competing with superconductivity in the cuprate superconductors and superconductor-(anti)ferromagnet heterostructures, competing ferromagnetic and antiferromagnetic orders in the spin glass/liquid systems, and competing topological trivial and non-trivial orders in the topological insulators. Researches on the sample morphology of cuprate superconductors already revealed percolation paths of superconducting region in a filamentary network [19]. Studying the domain topology is a way of examining the spin and charge fluctuation and the proximity effect. It would be interesting to try and generalize the study on domain topology in the fields mentioned above.

Appendix

The X-ray diffraction data from 11-ID-C, Advanced Photon Source of Argonne National Laboratory were collected in the form of intensity per pixel on the area detector during sample rotation. To obtain the structure factor from the data for single crystal Rietveld refinement, three important scale factors have to be removed from the data.

The first scale factor comes from the polarization of the X-ray beam. The electric field component parallel to the scattered wave vector cannot travel to the detector as radiation. Thus for X-rays polarized parallel to the scattering plane (the plane defined by the incident and scattered wave vectors), the intensity radiated to the detector is reduced by a factor of $\cos^2(2\theta)$ comparing to X-ray polarized perpendicular to the scattering plane. 11-ID-C uses unpolarized beam, so the scale factor becomes $(1+\cos^2(2\theta))/2$. Here 2θ is the scattering angle in Bragg's law.

The second scale factor, $\sin^{-1}(2\theta)$, comes from the *Jacobian* of changing from an angular basis in real space to the reciprocal lattice basis. Derivation can be found in X-Ray Diffraction by B. E. Warren. [145]

The third one depends on the angle between $\vec{G}_{hkl}$ and the sample rotation axis, i.e. ϕ_{hkl}. When the sample rotates by dα, $\vec{G}_{hkl}$ rotates by $\sin(\phi_{hkl})$dα accordingly. This leads to a scale factor of $1/\sin(\phi_{hkl})$ in the collected diffraction pattern. Removing it requires finding the rotation axis. This is achieved by taking the ratio between integrated intensity of same hkl reflections from the two configurations of *I4/m* phase. The structure factor cancels out, and the intensity ratio is proportional to the ratio of the scale factor and volume fraction of the two configurations, as shown in the following equation.

$$\frac{I_{hkl,1}}{I_{hkl,2}} \propto \frac{V_1}{V_2} \cdot \frac{\sin(\phi_0 + \varphi_{hkl,2})}{\sin(\phi_0 + \varphi_{hkl,1})} \tag{8.1}$$

Here the subscript 1 and 2 represent the two configurations. ϕ_0 defines the direction of the rotation axis. By tuning the angle ϕ_0, the best fitting on the reflections in HK0 plane is reached at $\phi_0 = -2.1^\circ$ with $Rsq = 0.97$.

The structure factor of reflections in the hk0 plane were obtained by integrating the peak intensities, removing the above scale factors then taking the square root. The two configurations of *I4/m* were combined into one *I4/m* phase. Single crystal refinement results based on these structure factors are listed in Table 5.1 and 5.2. In the non-superconducting sample, the Fe site occupancies are close to a perfect $\sqrt{5} \times \sqrt{5}$ vacancy order. On the other hand in the superconducting sample, the Fe2 site has an occupancy of $0.90(2)$, while the Fe1 site is almost empty. The partially occupied Fe2 site indicates partial order of the Fe vacancy. The correlation between occupancy and thermal factor is particularly strong when the site is almost empty. Therefore the refinement result of Fe2 occupancy is more reliable than the Fe1 occupancy. It is difficult to quantify the degree of partial order in the superconducting sample, but the difference in Fe2 occupation number clearly demonstrates that the annealed and quenched superconducting sample has vacancy disorder in the *I4/m* phase whereas the as-grown non-superconducting sample does not.

Bibliography

[1] Charles Kittel and Paul McEuen. *Introduction to solid state physics*. Wiley, 2018.

[2] Walter Greiner, Ludwig Neise, and Stöcker Horst. *Thermodynamics and statistical mechanics*. Springer-Verlag, 2004.

[3] *Physics of Condensed Matter*. Number v. 1. Springer-Verlag, 1963.

[4] E. Fermi. Zur quantelung des idealen einatomigen gases. *Zeitschrift für Physik*, 36(11):902–912, Nov 1926.

[5] Eduardo Fradkin. *Field theories of condensed matter physics*. Cambridge University Press, 2013.

[6] J. Zaanen, G. A. Sawatzky, and J. W. Allen. Band gaps and electronic structure of transition-metal compounds. *Phys. Rev. Lett.*, 55:418–421, Jul 1985.

[7] Susumu Yamada, Toshiyuki Imamura, and Masahiko Machida. High performance lobpcg method for solving multiple eigenvalues of hubbard model: Efficiency of communication avoiding neumann expansion preconditioner. In Rio Yokota and Weigang Wu, editors, *Supercomputing Frontiers*, pages 243–256, Cham, 2018. Springer International Publishing.

[8] J. Hubbard and Brian Hilton Flowers. Electron correlations in narrow energy bands. *Proceedings of the Royal Society of London. Series A. Mathematical and Physical Sciences*, 276(1365):238–257, 1963.

[9] R. B. Laughlin. Perspectives a critique of two metals. *Advances in Physics*, 47(6):943–958, 1998.

[10] A. Zylbersztejn and N. F. Mott. Metal-insulator transition in vanadium dioxide. *Phys. Rev. B*, 11:4383–4395, Jun 1975.

[11] Masatoshi Imada, Atsushi Fujimori, and Yoshinori Tokura. Metal-insulator transitions. *Rev. Mod. Phys.*, 70:1039–1263, Oct 1998.

[12] Eran Greenberg, Ivan Leonov, Samar Layek, Zuzana Konopkova, Moshe P. Pasternak, Leonid Dubrovinsky, Raymond Jeanloz, Igor A. Abrikosov, and Gregory Kh. Rozenberg. Pressure-induced site-selective mott insulator-metal transition in $\mathrm{Fe_2O_3}$. *Phys. Rev. X*, 8:031059, Sep 2018.

[13] Elbio Dagotto and Adriana Moreo. Phase diagram of the frustrated spin-1/2 Heisenberg antiferromagnet in 2 dimensions. *Phys. Rev. Lett.*, 63:2148–2151, Nov 1989.

[14] H. A. Ceccatto, C. J. Gazza, and A. E. Trumper. J_1-J_2 model: Energy, correlations, and order-parameter fluctuations on finite lattices. *Phys. Rev. B*, 45:7832–7836, Apr 1992.

[15] J. Sirker, Zheng Weihong, O. P. Sushkov, and J. Oitmaa. $J1-J2$ model: First-order phase transition versus deconfinement of spinons. *Phys. Rev. B*, 73:184420, May 2006.

[16] O. Mustonen, S. Vasala, K. P. Schmidt, E. Sadrollahi, H. C. Walker, I. Terasaki, F. J. Litterst, E. Baggio-Saitovitch, and M. Karppinen. Tuning the $\mathrm{S} = 1/2$ square-lattice antiferromagnet $\mathrm{Sr_2Cu(Te_{1-x}W_x)O_6}$ from Néel order to quantum disorder to columnar order. *Phys. Rev. B*, 98:064411, Aug 2018.

[17] Sami Vasala, Hassan Saadaoui, Elvezio Morenzoni, Omar Chmaissem, Ting-Shan Chan, Jin-Ming Chen, Ying-Ya Hsu, Hisao Yamauchi, and Maarit Karppinen. Characterization of magnetic properties of $\mathrm{Sr_2CuWO_6}$ and $\mathrm{Sr_2CuMoO_6}$. *Phys. Rev. B*, 89:134419, Apr 2014.

[18] P. Babkevich, Vamshi M. Katukuri, B. Fåk, S. Rols, T. Fennell, D. Pajić, H. Tanaka, T. Pardini, R. R. P. Singh, A. Mitrushchenkov, O. V. Yazyev, and H. M. Rønnow. Magnetic excitations and electronic interactions in $\mathrm{Sr_2CuTeO_6}$: A spin-$1/2$ square lattice Heisenberg antiferromagnet. *Phys. Rev. Lett.*, 117:237203, Dec 2016.

[19] G. Campi, A. Bianconi, N. Poccia, G. Bianconi, L. Barba, G. Arrighetti, D. Innocenti, J. Karpinski, N. D. Zhigadlo, S. M. Kazakov, and et al. Inhomogeneity of charge-density-wave order and quenched disorder in a high-T$_c$ superconductor. *Nature*, 525(7569):359–362, 2015.

[20] M. Fiebig, Th. Lottermoser, D. Fröhlich, A. V. Goltsev, and R. V. Pisarev. Observation of coupled magnetic and electric domains. *Nature*, 419(6909):818–820, 2002.

[21] Yoshihiro Ishibashi and Yutaka Takagi. Note on ferroelectric domain switching. *Journal of the Physical Society of Japan*, 31(2):506–510, 1971.

[22] M. Yamanouchi, D. Chiba, F. Matsukura, and H. Ohno. Current-induced domain-wall switching in a ferromagnetic semiconductor structure. *Nature*, 428(6982):539–542, 2004.

[23] Satoru Emori, Uwe Bauer, Sung-Min Ahn, Eduardo Martinez, and Geoffrey S. D. Beach. Current-driven dynamics of chiral ferromagnetic domain walls. *Nature Materials*, 12(7):611–616, 2013.

[24] H. K. Onnes. The resistance of pure mercury at helium temperatures. *Commun. Phys. Lab. Univ. Leiden.*, 12(120), 1911.

[25] R. C. Jaklevic, John Lambe, A. H. Silver, and J. E. Mercereau. Quantum interference effects in Josephson tunneling. *Phys. Rev. Lett.*, 12:159–160, Feb 1964.

[26] Ettore Majorana and Luciano Maiani. *A symmetric theory of electrons and positrons*, pages 201–233. Springer Berlin Heidelberg, Berlin, Heidelberg, 2006.

[27] Liang Fu and C. L. Kane. Superconducting proximity effect and Majorana fermions at the surface of a topological insulator. *Phys. Rev. Lett.*, 100:096407, Mar 2008.

[28] Jonathan De Roo. *The surface chemistry of metal oxide nanocrystals: from theory to applications*. PhD thesis, 01 2016.

[29] W. Meissner and R. Ochsenfeld. Ein neuer effekt bei eintritt der supraleitfähigkeit. *Die Naturwissenschaften*, 21(44):787–788, 1933.

[30] J. N. Rjabinin and L. W. Shubnikow. Magnetic properties and critical currents of supra-conducting alloys. *Nature*, 135(3415):581–582, 1935.

[31] Phillip W. Phillips Kenneth Chang. When superconductivity became clear (to some). *Physics Today*, 2008.

[32] V. L. Ginzburg and L. D. Landau. On the Theory of Superconductivity. *Zh. Eksp. Teor. Fiz.*, 20:1064–1082, 1950.

[33] A.A. Abrikosov. On the magnetic properties of superconductors of the second group. *Sov. Phys. JETP*, 5(1174), 1957.

[34] L.P. Gor'kov. Microscopic derivation of the Ginzburg-Landau equations in the theory of superconductivity. *Sov. Phys. JETP*, 9(1364), 1959.

[35] J. Bardeen, L. N. Cooper, and J. R. Schrieffer. Theory of superconductivity. *Phys. Rev.*, 108:1175–1204, Dec 1957.

[36] J. Bardeen, L. N. Cooper, and J. R. Schrieffer. Microscopic theory of superconductivity. *Phys. Rev.*, 106:162–164, Apr 1957.

[37] A. Hübsch and K. W. Becker. Renormalization of theelectron-phonon interaction: a reformulation of the BCS-gapequation. *The European Physical Journal B - Condensed Matter and Complex Systems*, 33(4):391–396, Jun 2003.

[38] Michael Tinkham. *Introduction to superconductivity*. Dover Publications, 2015.

[39] Adam Mann. High-temperature superconductivity at 25: Still in suspense. *Nature*, 475(7356):280–282, 2011.

[40] J. G. Bednorz and K. A. Müller. Possible high-Tc superconductivity in the Ba-La-Cu-O system. *Zeitschrift für Physik B Condensed Matter*, 64(2):189–193, Jun 1986.

[41] Pia Jensen Ray. *Master's thesis: Structural investigation of $La_{2-x}Sr_xCuO_{4+y}$ - Following staging as a function of temperature*. PhD thesis, Feb 2016.

[42] A. F. Hebard, M. J. Rosseinsky, R. C. Haddon, D. W. Murphy, S. H. Glarum, T. T. M. Palstra, A. P. Ramirez, and A. R. Kortan. Superconductivity at 18 K in potassium-doped C60. *Nature*, 350(6319):600–601, 1991.

[43] Yoichi Kamihara, Takumi Watanabe, Masahiro Hirano, and Hideo Hosono. Iron-based layered superconductor La[$O_{1-x}F_x$]FeAs (x = 0.05-0.12) with T_c = 26 K. *Journal of the American Chemical Society*, 130(11):3296–3297, 2008. PMID: 18293989.

[44] Jinsuk Song and James F. Annett. Electron-phonon coupling and d-wave superconductivity in the cuprates. *Phys. Rev. B*, 51:3840–3849, Feb 1995.

[45] P J Hirschfeld, M M Korshunov, and I I Mazin. Gap symmetry and structure of Fe-based superconductors. *Reports on Progress in Physics*, 74(12):124508, oct 2011.

[46] P. Monthoux, A. V. Balatsky, and D. Pines. Weak-coupling theory of high-temperature superconductivity in the antiferromagnetically correlated copper oxides. *Phys. Rev. B*, 46:14803–14817, Dec 1992.

[47] K. Terashima, Y. Sekiba, J. H. Bowen, K. Nakayama, T. Kawahara, T. Sato, P. Richard, Y.-M. Xu, L. J. Li, G. H. Cao, Z.-A. Xu, H. Ding, and T. Takahashi. Fermi surface nesting induced strong pairing in iron-based superconductors. *Proceedings of the National Academy of Sciences*, 106(18):7330–7333, 2009.

[48] Y. Xia, D. Qian, L. Wray, D. Hsieh, G. F. Chen, J. L. Luo, N. L. Wang, and M. Z. Hasan. Fermi surface topology and low-lying quasiparticle dynamics of parent $\mathrm{Fe}_{1+x}\mathrm{Te}/\mathrm{Se}$ superconductor. *Phys. Rev. Lett.*, 103:037002, Jul 2009.

[49] V. Brouet, M. Marsi, B. Mansart, A. Nicolaou, A. Taleb-Ibrahimi, P. Le Fèvre, F. Bertran, F. Rullier-Albenque, A. Forget, and D. Colson. Nesting between hole and electron pockets in $Ba(Fe_{1-x}Co_x)_2As_2$ $(x = 0 - 0.3)$ observed with angle-resolved photoemission. *Phys. Rev. B*, 80:165115, Oct 2009.

[50] Louis Taillefer. Scattering and pairing in cuprate superconductors. *Annual Review of Condensed Matter Physics*, 1, 03 2010.

[51] Johnpierre Paglione and Richard L. Greene. High-temperature superconductivity in iron-based materials. *Nature Physics*, 6(9):645–658, 2010.

[52] Pengcheng Dai, Jiangping Hu, and Elbio Dagotto. Magnetism and its microscopic origin in iron-based high-temperature superconductors. *Nature Physics*, 8(10):709–718, 2012.

[53] Igor I. Mazin. Superconductivity gets an iron boost. *Nature*, 464(7286):183–186, 2010.

[54] T. Qian, X.-P. Wang, W.-C. Jin, P. Zhang, P. Richard, G. Xu, X. Dai, Z. Fang, J.-G. Guo, X.-L. Chen, and H. Ding. Absence of a holelike fermi surface for the iron-based $K_{0.8}Fe_{1.7}Se_2$ superconductor revealed by angle-resolved photoemission spectroscopy. *Phys. Rev. Lett.*, 106:187001, May 2011.

[55] Chunruo Duan, Junjie Yang, Feng Ye, and Despina Louca. Evidence of nematicity in $K_{0.8}Fe_{1.7}Se_2$. *Journal of Superconductivity and Novel Magnetism*, 29(3):663–666, Mar 2016.

[56] S. Kasahara, H. J. Shi, K. Hashimoto, S. Tonegawa, Y. Mizukami, T. Shibauchi, K. Sugimoto, T. Fukuda, T. Terashima, Andriy H. Nevidomskyy, and et al. Electronic nematicity above the structural and superconducting transition in $BaFe_2(As_{1-x}P_x)_2$. *Nature*, 486(7403):382–385, 2012.

[57] Wei Bao, Qing-Zhen Huang, Gen-Fu Chen, Du-Ming Wang, Jun-Bao He, and Yi-Ming Qiu. A novel large moment antiferromagnetic order in $K_{0.8}Fe_{1.6}Se_2$ superconductor. *Chinese Physics Letters*, 28(8):086104, 2011.

[58] Y. J. Yan, M. Zhang, A. F. Wang, J. J. Ying, Z. Y. Li, W. Qin, X. G. Luo, J. Q. Li, Jiangping Hu, X. H. Chen, and et al. Electronic and magnetic phase diagram in $K_xFe_{2-y}Se_2$ superconductors. *Scientific Reports*, 2(212), 2012.

[59] Xiaxin Ding, Delong Fang, Zhenyu Wang, Huan Yang, Jianzhong Liu, Qiang Deng, Guobin Ma, Chong Meng, Yuhui Hu, Hai-Hu Wen, and et al. Influence of microstructure on superconductivity in $K_xFe_{2-y}Se_2$ and evidence for a new parent phase $K_2Fe_7Se_8$. *Nature Communications*, 4(1897), 2013.

[60] Scott V. Carr, Despina Louca, Joan Siewenie, Q. Huang, Aifeng Wang, Xianhui Chen, and Pengcheng Dai. Structure and composition of the superconducting phase in alkali iron selenide $K_yFe_{1.6+x}Se_2$. *Phys. Rev. B*, 89:134509, Apr 2014.

[61] Malcolm E. Lines and Alastair M. Glass. *Principles and applications of ferroelectrics and related materials*. Clarendon Press, 2009.

[62] Chikazumi Soshin. *Physics of ferromagnetism*. Oxford Univ. Press, 2010.

[63] Ekhard K.H. Salje. Ferroelastic materials. *Annual Review of Materials Research*, 42(1):265–283, 2012.

[64] G. H. Kwei, A. C. Lawson, S. J. L. Billinge, and S. W. Cheong. Structures of the ferroelectric phases of barium titanate. *The Journal of Physical Chemistry*, 97(10):2368–2377, 1993.

[65] J. Shieh, J.H. Yeh, Y.C. Shu, and J.H. Yen. Hysteresis behaviors of barium titanate single crystals based on the operation of multiple 90° switching systems. *Materials Science and Engineering: B*, 161(1):50 – 54, 2009. Proceedings of the joint meeting of the 2nd International Conference on the Science and Technology for Advanced Ceramics (STAC-II) and the 1st International Conference on the Science and Technology of Solid Surfaces and Interfaces (STSI-I).

[66] A. von Hippel. Ferroelectricity, domain structure, and phase transitions of barium titanate. *Rev. Mod. Phys.*, 22:221–237, Jul 1950.

[67] Sang-Wook Cheong and Maxim Mostovoy. Multiferroics: a magnetic twist for ferroelectricity. *Nature Materials*, 6(1):13–20, 2007.

[68] N. A. Spaldin. MATERIALS SCIENCE: The renaissance of magnetoelectric multiferroics. *Science*, 309(5733):391–392, 2005.

[69] Manfred Fiebig. Revival of the magnetoelectric effect. *Journal of Physics D: Applied Physics*, 38(8):R123–R152, apr 2005.

[70] T. Kimura, T. Goto, H. Shintani, K. Ishizaka, T. Arima, and Y. Tokura. Magnetic control of ferroelectric polarization. *Nature*, 426(6962):55–58, 2003.

[71] N. Hur, S. Park, P. A. Sharma, J. S. Ahn, S. Guha, and S-W. Cheong. Electric polarization reversal and memory in a multiferroic material induced by magnetic fields. *Nature*, 429(6990):392–395, 2004.

[72] Daniel Khomskii. Classifying multiferroics: Mechanisms and effects. *Physics*, 2(20), Sep 2009.

[73] J. Wang, J. B. Neaton, H. Zheng, V. Nagarajan, S. B. Ogale, B. Liu, D. Viehland, V. Vaithyanathan, D. G. Schlom, U. V. Waghmare, N. A. Spaldin, K. M. Rabe, M. Wuttig, and R. Ramesh. Epitaxial $BiFeO_3$ multiferroic thin film heterostructures. *Science*, 299(5613):1719–1722, 2003.

[74] D.m. Evans, A. Schilling, Ashok Kumar, D. Sanchez, N. Ortega, M. Arredondo, R.s. Katiyar, J.m. Gregg, and J.f. Scott. Magnetic switching of ferroelectric domains at room temperature in multiferroic PZTFT. *Nature Communications*, 4(1), 2013.

[75] H. L. Yakel Jnr, W. C. Koehler, E. F. Bertaut, and E. F. Forrat. On the crystal structure of the manganese(III) trioxides of the heavy lanthanides and yttrium. *Acta Crystallographica*, 16(10):957–962, Oct 1963.

[76] T. Choi, Y. Horibe, H. T. Yi, Y. J. Choi, Weida Wu, and S.-W. Cheong. Insulating interlocked ferroelectric and structural antiphase domain walls in multiferroic $YMnO_3$. *Nature Materials*, 9(3):253–258, 2010.

[77] Y. Aikawa, T. Katsufuji, T. Arima, and K. Kato. Effect of Mn trimerization on the magnetic and dielectric properties of hexagonal $YMnO_3$. *Phys. Rev. B*, 71:184418, May 2005.

[78] K. Taniguchi, N. Abe, T. Takenobu, Y. Iwasa, and T. Arima. Ferroelectric polarization flop in a frustrated magnet $MnWO_4$ induced by a magnetic field. *Phys. Rev. Lett.*, 97:097203, Aug 2006.

[79] T. Katsufuji, S. Mori, M. Masaki, Y. Moritomo, N. Yamamoto, and H. Takagi. Dielectric and magnetic anomalies and spin frustration in hexagonal $RMnO_3$ (R=Y, Yb, and Lu). *Phys. Rev. B*, 64:104419, Aug 2001.

[80] T. Kimura, S. Kawamoto, I. Yamada, M. Azuma, M. Takano, and Y. Tokura. Magnetocapacitance effect in multiferroic $BiMnO_3$. *Phys. Rev. B*, 67:180401, May 2003.

[81] Ram Seshadri and Nicola A. Hill. Visualizing the role of Bi 6s "lone pairs" in the off-center distortion in ferromagnetic $BiMnO_3$. *Chemistry of Materials*, 13(9):2892–2899, 2001.

[82] G. Lawes, A. B. Harris, T. Kimura, N. Rogado, R. J. Cava, A. Aharony, O. Entin-Wohlman, T. Yildirim, M. Kenzelmann, C. Broholm, and A. P. Ramirez. Magnetically driven ferroelectric order in $Ni_3V_2O_8$. *Phys. Rev. Lett.*, 95:087205, Aug 2005.

[83] Claudine Lacroix, Philippe Mendels, and Mila Frédéric. *Introduction to Frustrated Magnetism Materials, Experiments, Theory*. Springer Berlin, 2013.

[84] I. Dzyaloshinsky. A thermodynamic theory of "weak" ferromagnetism of antiferromagnetics. *Journal of Physics and Chemistry of Solids*, 4(4):241 – 255, 1958.

[85] Tôru Moriya. Anisotropic superexchange interaction and weak ferromagnetism. *Phys. Rev.*, 120:91–98, Oct 1960.

[86] M. Bode, M. Heide, K. Von Bergmann, P. Ferriani, S. Heinze, G. Bihlmayer, A. Kubetzka, O. Pietzsch, S. Blügel, R. Wiesendanger, and et al. Chiral magnetic order at surfaces driven by inversion asymmetry. *Nature*, 447(7141):190–193, 2007.

[87] Stefan Heinze, Kirsten Von Bergmann, Matthias Menzel, Jens Brede, André Kubetzka, Roland Wiesendanger, Gustav Bihlmayer, and Stefan Blügel. Spontaneous atomic-scale magnetic skyrmion lattice in two dimensions. *Nature Physics*, 7(9):713–718, 2011.

[88] Hosho Katsura, Naoto Nagaosa, and Alexander V. Balatsky. Spin current and magnetoelectric effect in noncollinear magnets. *Phys. Rev. Lett.*, 95:057205, Jul 2005.

[89] I. A. Sergienko and E. Dagotto. Role of the Dzyaloshinskii-Moriya interaction in multiferroic perovskites. *Phys. Rev. B*, 73:094434, Mar 2006.

[90] Chunruo Duan, Gia-Wei Chern, and Despina Louca. A monte-carlo study on the coupling of magnetism and ferroelectricity in the hexagonal multiferroic $RMnO_3$. *Condensed Matter*, 3(4), 2018.

[91] Chunruo Duan, Junjie Yang, Yang Ren, Sean M. Thomas, and Despina Louca. Appearance of superconductivity at the vacancy order-disorder boundary in $K_xFe_{2-y}Se_2$. *Phys. Rev. B*, 97:184502, May 2018.

[92] Chunruo Duan and Despina Louca. Fe vacancy order and domain distribution in $A_xFe_{2-y}Se_2$. *Journal of Superconductivity and Novel Magnetism*, 31(3):757–761, Mar 2018.

[93] William Barlow. Probable nature of the internal symmetry of crystals. *Nature*, 29(738):186–188, 1883.

[94] Martin Attfield, Paul Barnes, Jeremy Cockcroft, and Huub Driessen. Advanced certificate in powder diffraction on the web. *http://pd.chem.ucl.ac.uk/pdnn/pdindex.htm*, 2006.

[95] H. M. Rietveld. A profile refinement method for nuclear and magnetic structures. *Journal of Applied Crystallography*, 2(2):65–71, Jun 1969.

[96] J. F. Ramaley. Buffon's noodle problem. *The American Mathematical Monthly*, 76(8):916–918, 1969.

[97] K. Binder. *Ising Model in Encyclopédia of mathemati*. London: Academic Press Inc, 2008.

[98] A. N. Pirogov. Polarization in $RMnO_3$ multiferroics. *Acta Crystallographica Section B*, 72(1):1–2, Feb 2016.

[99] R Feyerherm, E Dudzik, O Prokhnenko, and D N Argyriou. Rare earth magnetism and ferroelectricity RMnO3. *Journal of Physics: Conference Series*, 200(1):012032, jan 2010.

[100] T. Katsufuji, S. Mori, M. Masaki, Y. Moritomo, N. Yamamoto, and H. Takagi. Dielectric and magnetic anomalies and spin frustration in hexagonal $RMnO_3$ (R=Y, Yb, and Lu). *Phys. Rev. B*, 64:104419, Aug 2001.

[101] D G Tomuta, S Ramakrishnan, G J Nieuwenhuys, and J A Mydosh. The magnetic susceptibility, specific heat and dielectric constant of hexagonal $YMnO_3$, $LuMnO_3$ and $ScMnO_3$. *Journal of Physics: Condensed Matter*, 13(20):4543–4552, Apr 2001.

[102] A. Muñoz, J. A. Alonso, M. J. Martínez-Lope, M. T. Casáis, J. L. Martínez, and M. T. Fernández-Díaz. Magnetic structure of hexagonal $RMnO_3$ (R=Y, Sc): Thermal evolution from neutron powder diffraction data. *Phys. Rev. B*, 62:9498–9510, Oct 2000.

[103] Junjie Yang, Chunruo Duan, John R. D. Copley, Craig M. Brown, and Despina Louca. The magnetic transitions and dynamics in the multiferroic $Lu_{0.5}Sc_{0.5}FeO_3$. *MRS Advances*, 1(9):565–571, 2016.

[104] I. V. Solovyev, M. V. Valentyuk, and V. V. Mazurenko. Magnetic structure of hexagonal $YMnO_3$ and $LuMnO_3$ from a microscopic point of view. *Phys. Rev. B*, 86:054407, Aug 2012.

[105] Kiran Singh, Marie-Bernadette Lepetit, Charles Simon, Natalia Bellido, Stéphane Pailhès, Julien Varignon, and Albin De Muer. Analysis of the multiferroicity in the hexagonal manganite YMnO3. *Journal of Physics: Condensed Matter*, 25(41):416002, sep 2013.

[106] W. Tian, Guotai Tan, Liu Liu, Jinxing Zhang, Barry Winn, Tao Hong, J. A. Fernandez-Baca, Chenglin Zhang, and Pengcheng Dai. Influence of doping on the spin dynamics and magnetoelectric effect in hexagonal $Y_{0.7}Lu_{0.3}MnO_3$. *Phys. Rev. B*, 89:144417, Apr 2014.

[107] Thomas Lottermoser, Thomas Lonkai, Uwe Amann, Dietmar Hohlwein, Jörg Ihringer, and Manfred Fiebig. Magnetic phase control by an electric field. *Nature*, 430(6999):541–544, 2004.

[108] J. Li, H. X. Yang, H. F. Tian, C. Ma, S. Zhang, Y. G. Zhao, and J. Q. Li. Scanning secondary-electron microscopy on ferroelectric domains and domain walls in $YMnO_3$. *Applied Physics Letters*, 100(15):152903, Sep 2012.

[109] S. C. Chae, N. Lee, Y. Horibe, M. Tanimura, S. Mori, B. Gao, S. Carr, and S.-W. Cheong. Direct observation of the proliferation of ferroelectric loop domains and vortex-antivortex pairs. *Phys. Rev. Lett.*, 108:167603, Apr 2012.

[110] S. C. Chae, Y. Horibe, D. Y. Jeong, N. Lee, K. Iida, M. Tanimura, and S.-W. Cheong. Evolution of the domain topology in a ferroelectric. *Phys. Rev. Lett.*, 110:167601, Apr 2013.

[111] Stephen E. Rowley and Gilbert G. Lonzarich. Ferroelectrics in a twist. *Nature Physics*, 10(12):907–908, 2014.

[112] Shi-Zeng Lin, Xueyun Wang, Yoshitomo Kamiya, Gia-Wei Chern, Fei Fan, David Fan, Brian Casas, Yue Liu, Valery Kiryukhin, Wojciech H. Zurek, and et al. Topological defects as relics of emergent continuous symmetry and Higgs condensation of disorder in ferroelectrics. *Nature Physics*, 10(12):970?977, 2014.

[113] J M Kosterlitz and D J Thouless. Ordering, metastability and phase transitions in two-dimensional systems. *Journal of Physics C: Solid State Physics*, 6(7):1181, 1973.

[114] J L Cardy. General discrete planar models in two dimensions: Duality properties and phase diagrams. *Journal of Physics A: Mathematical and General*, 13(4):1507–1515, Jan 1980.

[115] Gia-Wei Chern and Oleg Tchernyshyov. Magnetic charge and ordering in kagome spin ice. *Philosophical Transactions of the Royal Society of London A: Mathematical, Physical and Engineering Sciences*, 370(1981):5718–5737, 2012.

[116] Murty S. S. Challa and D. P. Landau. Critical behavior of the six-state clock model in two dimensions. *Phys. Rev. B*, 33:437–443, Jan 1986.

[117] R. Skulski. Superparaelectric behaviours of relaxor ferroelectrics. *Materials Science and Engineering: B*, 64(1):39 – 43, 1999.

[118] L. Eric Cross. Relaxor ferroelectrics. *Ferroelectrics*, 76(1):241–267, 1987.

[119] S. H. Skjærvø, Q. Meier, M. Feygenson, N. A. Spaldin, S. J. L. Billinge, E. S. Bozin, and S. M. Selbach. Unconventional order-disorder phase transition in improper ferroelectric hexagonal manganites. *ArXiv e-prints*, July 2017.

[120] X. Wang, M. Mostovoy, M. G. Han, Y. Horibe, T. Aoki, Y. Zhu, and S.-W. Cheong. Unfolding of vortices into topological stripes in a multiferroic material. *Phys. Rev. Lett.*, 112:247601, Jun 2014.

[121] Sergey Artyukhin, Kris T. Delaney, Nicola A. Spaldin, and Maxim Mostovoy. Landau theory of topological defects in multiferroic hexagonal manganites. *Nature Materials*, 13(1):42–49, 2013.

[122] S. Petit, F. Moussa, M. Hennion, S. Pailhès, L. Pinsard-Gaudart, and A. Ivanov. Spin phonon coupling in hexagonal multiferroic $\mathrm{YMnO_3}$. *Phys. Rev. Lett.*, 99:266604, Dec 2007.

[123] Mario Poirier, Francis Laliberté, Loreynne Pinsard-Gaudart, and Alexandre Revcolevschi. Magnetoelastic coupling in hexagonal multiferroic $\mathrm{YMnO_3}$ using ultrasound measurements. *Phys. Rev. B*, 76:174426, Nov 2007.

[124] S F Edwards and P W Anderson. Theory of spin glasses. *Journal of Physics F: Metal Physics*, 5(5):965, 1975.

[125] Jiangang Guo, Shifeng Jin, Gang Wang, Shunchong Wang, Kaixing Zhu, Tingting Zhou, Meng He, and Xiaolong Chen. Superconductivity in the iron selenide $K_xFe_2Se_2$ $(0 \leq x \leq 1.0)$. *Phys. Rev. B*, 82:180520, Nov 2010.

[126] Wei Bao, Guan-Nan Li, Qing-Zhen Huang, Gen-Fu Chen, Jun-Bao He, Du-Ming Wang, M. A. Green, Yi-Ming Qiu, Jian-Lin Luo, Mei-Mei Wu, and et al. Superconductivity tuned by the iron vacancy order in $K_xFe_{2-y}Se_2$. *Chinese Physics Letters*, 30(2):027402, 2013.

[127] Alessandro Ricci, Nicola Poccia, Boby Joseph, Gianmichele Arrighetti, Luisa Barba, Jasper Plaisier, Gaetano Campi, Yoshikazu Mizuguchi, Hiroyuki Takeya, Yoshihiko Takano, and et al. Intrinsic phase separation in superconducting $K_{0.8}Fe_{1.6}Se_2$ (T_c= 31.8 K) single crystals. *Superconductor Science and Technology*, 24(8):082002, 2011.

[128] A. Ricci, N. Poccia, G. Campi, B. Joseph, G. Arrighetti, L. Barba, M. Reynolds, M. Burghammer, H. Takeya, Y. Mizuguchi, Y. Takano, M. Colapietro, N. L. Saini, and A. Bianconi. Nanoscale phase separation in the iron chalcogenide superconductor $K_{0.8}Fe_{1.6}Se_2$ as seen via scanning nanofocused x-ray diffraction. *Phys. Rev. B*, 84:060511, Aug 2011.

[129] Wei Li, Hao Ding, Peng Deng, Kai Chang, Canli Song, Ke He, Lili Wang, Xucun Ma, Jiang-Ping Hu, Xi Chen, and et al. Phase separation and magnetic order in K-doped iron selenide superconductor. *Nature Physics*, 8(2):126–130, 2011.

[130] R. H. Yuan, T. Dong, Y. J. Song, P. Zheng, G. F. Chen, J. P. Hu, J. Q. Li, and N. L. Wang. Nanoscale phase separation of antiferromagnetic order and superconductivity in $K_{0.75}Fe_{1.75}Se_2$. *Scientific Reports*, 2(221), 2012.

[131] F. Ye, S. Chi, Wei Bao, X. F. Wang, J. J. Ying, X. H. Chen, H. D. Wang, C. H. Dong, and Minghu Fang. Common crystalline and magnetic structure of superconducting $\mathrm{A_2Fe_4Se_5}$ $(\mathrm{A = K, Rb, Cs, Tl})$ single crystals measured using neutron diffraction. *Phys. Rev. Lett.*, 107:137003, Sep 2011.

[132] P. Zavalij, Wei Bao, X. F. Wang, J. J. Ying, X. H. Chen, D. M. Wang, J. B. He, X. Q. Wang, G. F. Chen, P.-Y. Hsieh, Q. Huang, and M. A. Green. Structure of vacancy-ordered single-crystalline superconducting potassium iron selenide. *Phys. Rev. B*, 83:132509, Apr 2011.

[133] Z. Wang, Y. J. Song, H. L. Shi, Z. W. Wang, Z. Chen, H. F. Tian, G. F. Chen, J. G. Guo, H. X. Yang, and J. Q. Li. Microstructure and ordering of iron vacancies in the superconductor system $K_yFe_xSe_2$ as seen via transmission electron microscopy. *Phys. Rev. B*, 83:140505, Apr 2011.

[134] Sergey M. Kazakov, Artem M. Abakumov, Santiago González, Juan Manuel Perez-Mato, Alexander V. Ovchinnikov, Maria V. Roslova, Alexander I. Boltalin, Igor V. Morozov, Evgeny V. Antipov, Gustaaf Van Tendeloo, and et al. Uniform patterns of fe-vacancy ordering in the $K_x(Fe,Co)_{2-y}Se_2$ superconductors. *Chemistry of Materials*, 23(19):4311–4316, 2011.

[135] Y. Zhang, L. X. Yang, M. Xu, Z. R. Ye, F. Chen, C. He, H. C. Xu, J. Jiang, B. P. Xie, J. J. Ying, and et al. Nodeless superconducting gap in $A_xFe_2Se_2$ (A=K,Cs) revealed by angle-resolved photoemission spectroscopy. *Nature Materials*, 10(4):273–277, 2011.

[136] A. Bosak, V. Svitlyk, A. Krzton-Maziopa, E. Pomjakushina, K. Conder, V. Pomjakushin, A. Popov, D. de Sanctis, and D. Chernyshov. Phase coexistence in $Cs_{0.8}Fe_{1.6}Se_2$ as seen by x-ray mapping of reciprocal space. *Phys. Rev. B*, 86:174107, Nov 2012.

[137] K. M. Taddei, M. Sturza, D. Y. Chung, H. B. Cao, H. Claus, M. G. Kanatzidis, R. Osborn, S. Rosenkranz, and O. Chmaissem. Cesium vacancy ordering in phase-separated $Cs_xFe_{2-y}Se_2$. *Phys. Rev. B*, 92:094505, Sep 2015.

[138] D. G. Porter, E. Cemal, D. J. Voneshen, K. Refson, M. J. Gutmann, A. Bombardi, A. T. Boothroyd, A. Krzton-Maziopa, E. Pomjakushina, K. Conder, and J. P. Goff. Two-dimensional cs-vacancy superstructure in iron-based superconductor $Cs_{0.8}Fe_{1.6}Se_2$. *Phys. Rev. B*, 91:144114, Apr 2015.

[139] Fei Han, Huan Yang, Bing Shen, Zhen-Yu Wang, Chun-Hong Li, and Hai-Hu Wen. Metastable superconducting state in quenched $K_xFe_{2-y}Se_2$. *Philosophical Magazine*, 92(19-21):2553–2562, 2012.

[140] Hyejin Ryu, Hechang Lei, A. I. Frenkel, and C. Petrovic. Local structural disorder and superconductivity in $K_xFe_{2-y}Se_2$. *Phys. Rev. B*, 85:224515, Jun 2012.

[141] J. Yang, C. Duan, Q. Huang, C. Brown, J. Neuefeind, and Despina Louca. Strong correlations between vacancy and magnetic ordering in superconducting $K_{0.8}Fe_{2-y}Se_2$. *Phys. Rev. B*, 94:024503, Jul 2016.

[142] M. Bendele, A. Barinov, B. Joseph, D. Innocenti, A. Iadecola, A. Bianconi, H. Takeya, Y. Mizuguchi, Y. Takano, T. Noji, and et al. Spectromicroscopy of electronic phase separation in $K_xFe_{2-y}Se_2$ superconductor. *Scientific Reports*, 4(5592), 2014.

[143] Tom Berlijn, P. J. Hirschfeld, and Wei Ku. Effective doping and suppression of Fermi surface reconstruction via Fe vacancy disorder in $K_xFe_{2-y}Se_2$. *Phys. Rev. Lett.*, 109:147003, Oct 2012.

[144] A. Schilling, M. Cantoni, J. D. Guo, and H. R. Ott. Superconductivity above 130 K in the Hg–Ba–Ca–Cu–O system. *Nature*, 363(6424):56–58, 1993.

[145] B.E. Warren. *X-ray Diffraction*. Addison-Wesley series in metallurgy and materials engineering. Dover Publications, 1990.